energies

MDPI

Article

A Heuristic Approach to Optimal Crowbar Setting and Low Voltage Ride through of a Doubly Fed Induction Generator

Kumeshan Reddy and Akshay Kumar Saha *

Discipline of Electrical, Electronic and Computer Engineering, University of KwaZulu-Natal, Durban 4041, South Africa
* Correspondence: saha@ukzn.ac.za

Abstract: In this paper, a heuristic approach to doubly fed induction generator (DFIG) protection and low voltage ride through (LVRT) is carried out. DFIG-based wind systems are rapidly penetrating the power generation section. Despite their advantages, their direct coupling grid makes them highly sensitive to symmetrical faults. A well-known solution to this is the crowbar method of DFIG protection. This paper provides a method to determine the optimal crowbar resistance value, to ensure a strong trade-off between the rotor current and DC voltage transients. Further, since the crowbar method requires disconnection from the grid, the linear quadratic regulator (LQR) is applied to the system. This is to ensure fault ride through compliance with recent grid code requirements. The well-known PSO, as well as the recently developed African vultures optimization algorithm (AVOA), was applied to the problem. The first set of results show that for severe symmetrical voltage dips, the AVOA provides a good option for crowbar magnitude optimization, whereas PSO performed better for moderately severe dips. Secondly, when the LQR was optimized via the AVOA, it exhibited superiority over the conventional PSO-based PI controller. This superiority was in terms of rotor current transient magnitude, DC voltage transient magnitude, and reactive power steady-state ripple and were in the order of 67.5%, 20.35%, and 37.55%, respectively. When comparing the crowbar method and the LQR, it was observed that despite the LQR exhibiting superiority in terms of transient performance, the crowbar method offered a unanimously superior settling time.

Keywords: doubly fed induction generator; optimization methods; algorithms; crowbar; linear quadratic regulator

Citation: Reddy, K.; Saha, A.K. A Heuristic Approach to Optimal Crowbar Setting and Low Voltage Ride through of a Doubly Fed Induction Generator. *Energies* **2022**, *15*, 9307. https://doi.org/10.3390/en15249307

Academic Editor: Ahmed Abu-Siada

Received: 12 November 2022
Accepted: 6 December 2022
Published: 8 December 2022

1. Introduction

The use of grid-connected wind energy conversion systems has seen a drastic rise in the past two decades. This can be attributed to the rugged and robust performance of synchronous and asynchronous generators [1]. In particular, the doubly fed induction generator has been the machine of choice. This is largely due to factors such as direct grid connection (thereby persevering grid inertia) and the use of only a partially rated power electronic converter [1]. The structure of the DFIG can be observed in Figure 1 [2]. Owing to its various merits, the DFIG has recently come under intense investigation. An example of this is [1,3], whereby the authors analyzed the effect of applying model predictive control to the DFIG, to analyze response time and stead-state characteristics. Another example can be found in [4], where the authors utilized a novel model predictive control method to achieve stringent load frequency control.

However, despite its many advantages, this direct grid connection has its drawbacks. In the case of a three-phase short-circuit fault, the DFIG reacts sensitively [5,6]. The abrupt change in grid voltage magnitude creates a large transient stator flux [5]. This has the potential to cause drastic overvoltage and overcurrent in the rotor side of the DFIG [5,6]. A common approach to preventing these catastrophic consequences would be to short-circuit the rotor via the use of a crowbar [5,7–9]. While this works well, the optimal sizing

of the crowbar resistance is challenging. A small crowbar resistance ensures a smaller rotor voltage, but a large spike in the rotor current. Similarly, a large crowbar resistance successfully limits the rotor current, but at the expense of an overvoltage. This is observed in Figures 2 and 3. Therefore, optimal sizing of the crowbar circuit is essential.

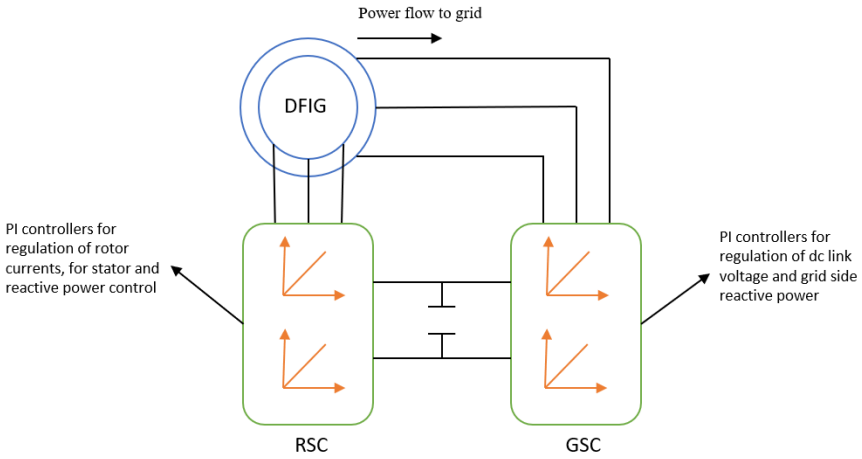

Figure 1. General structure of DFIG [2].

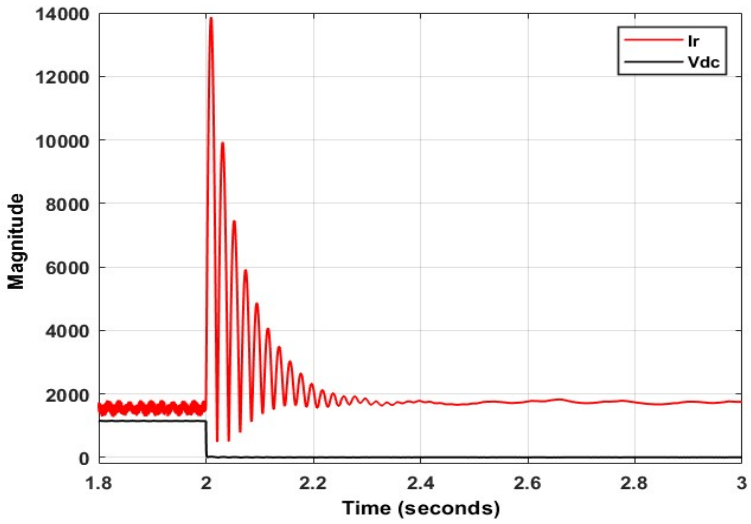

Figure 2. Rotor response with a 0.001 Ω crowbar.

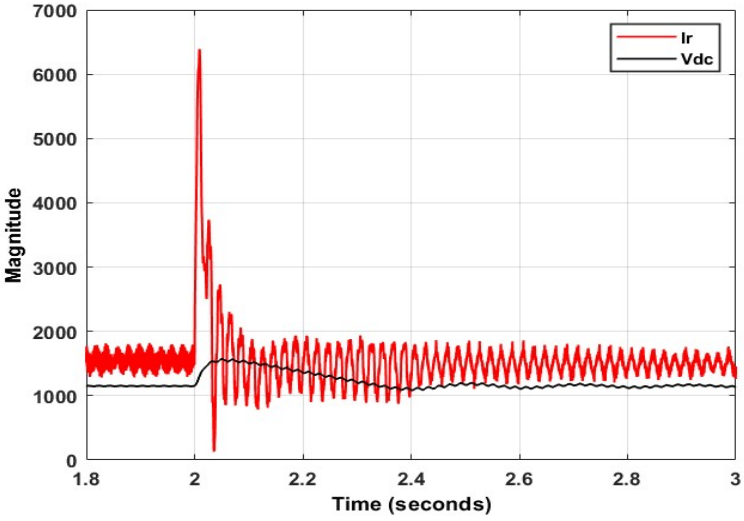

Figure 3. Rotor response with a 20 Ω crowbar.

The authors in [5] devised a method to determine the minimum and maximum value of the crowbar resistance. This considered both the maximum rotor voltage and maximum rotor current. Then, various values within this predetermined range were investigated. However, despite the rotor DC voltage being kept below its threshold, the best-case rotor current still exceeded 5 p.u. A similar approach was followed in [7], where the effects of varying the crowbar resistance was clearly depicted. An analytical hierarchy process-based algorithm was utilized in [10] to determine the optimal crowbar resistance. Once again, the rotor current reached unacceptable values of over 6 p.u. The method outlined in [11] makes use of thyristors to control the firing of the crowbar. The study emphasizes the effect of the crowbar resistance on the DC voltage but does not consider the rotor side current. Further, the study was not comprehensive. A study conducted in [12] analyzed the effect of rotor speed of the DFIG during grid faults. However, the study did not consider the rotor side current. The work presented in [13] made use of controllable series crowbar resistors. The resistors were activated via circuit breakers, utilizing the ANFIS system. The value of the crowbar resistors was calculated based on a multiplying factor of the stator resistance. However, as like other research presented, no effect of the fault on the rotor side current was analyzed.

2. Motivation and Contribution

Despite the crowbar approach working well in the reduction of rotor voltage and current transients, it has a major disadvantage; the crowbar resistances consume reactive power [7,14]. Due to the continuous penetration of wind energy conversion systems to grids throughout the world, numerous nations have revised their grid code. Now, in the case of a three-phase grid voltage sag, WECS are required to remain connected to the grid and provide reactive power to ensure timeous restoration of the grid voltage. A common and established approach is to utilize a method called a demagnetizing current injection [15]. Considering that during the presence of a symmetrical voltage drip, the stator flux comprises both a natural and forced component, the demagnetizing current injection scheme works by estimating the induced natural flux, and then proceeds to eliminate such. The estimated natural flux, coupled with a negative gain, is fed into the respective rotor current reference. Owing to the initial success of the control strategy, various modifications have been proposed. The authors in [16] make use of the demagnetizing current to damp the DC component of the stator flux, as well as a passive switchable circuit to reduce the time constant and subsequent duration of the transient flux. The method presented in [17] makes use of both the crowbar and an optimized demagnetizing co-efficient to comply with grid code requirement. A robust control strategy was explained in [18], which utilizes explicit model predictive control to provide continuous adjustment of the demagnetizing current coefficient. A stator-connected dynamic volage restorer, with a rotor-connected inductor-based fault current limiter, was proposed in [19]. The method efficiently limited the rotor current transient, as well as the DC voltage peak. However, no insight on the reactive power was provided. The authors in [20] utilized fuzzy logic controllers to enhance the reactive power injection of the DFIG. While proving to be successful in achieving reactive power supply, the method did not analyze the effects of the control circuit on the rotor current transient and DC voltage magnitudes.

Apart from the above-mentioned techniques, various other methods are explained in [21]. One such method is the utilization of a DC chopper. In this method, a power electronic switch is used to control the current flowing through a braking resistor. This method successfully limits the DC voltage, but in its conventional form, cannot limit the rotor current transient. Another method is the use of a series dynamic resistor, which is placed between the rotor terminals of the DFIG and the rotor side converter. This method, however, proved to be inferior to the crowbar protection scheme. As of recent times, the linear quadratic regulator has come under investigation for the purpose of LVRT of the DFIG. The authors in [22] utilized the LQR in place of the conventional PI controller, for stator flux-oriented vector control. The gains of the controller were optimized using a

genetic algorithm. The controller produced good results but was only tested at a voltage dip of 50%. The LQR was optimized using PSO in [23], but this was only tested at steady-state response. A study conducted in [24] compared the efficacy of a GA-optimized LQR with the conventional LQR optimization method. However, only a 10% reduction in the grid voltage was tested. A relatively new optimization technique, called the mean variance mapping optimization algorithm, was proposed in [25] to optimize the gains of the LQR controller. The results were compared to that of the PI controller and proved to be superior. However, the machine was operated only in super synchronous mode, and only a voltage dip of 90% was evaluated. Further, evaluation of the post-fault steady-state error was not conducted. Lastly, the effect on transient rotor current was not clearly expressed.

As evident, the effects of crowbar circuits on the DFIG have been well investigated. However, there still exists a lack of optimal crowbar setting to ensure an adequate trade-off between the rotor side current and DC voltage. Further, owing to the continuous penetration of wind farms into the national grid, and subsequent stringent levels of grid codes, there is a dire need to improve fault ride through the capabilities of the DFIG. The promising results via utilization of the LQR makes this an attractive control method to mitigate the effects of symmetrical voltage dips. Thus far, it is evident that metaheuristic optimization techniques have been applied to LQR optimization. PSO, GA, and MVMO has thus far produced promising results. However, there still exists a deficiency of thorough investigation of results. Since their inception, metaheuristic optimization techniques have undergone various enhancements, and many new state-of-the-art optimization techniques were subsequently developed. This paper provides a novel application of the African vultures optimization algorithm for control of the DFIG during the case of symmetrical voltage dips. AVOA is a new swarm-based optimization technique, based on the social and feeding behavior of the various species of African vultures. Being a swarm intelligence technique, this algorithm is simple in structure. Further, as validated by the proposed authors, the algorithm exhibits strong exploration, exploitation, and convergence rate capabilities [26]. The algorithm is applied to achieve both optimal crowbar magnitude, as well as optimal gains for a LQR controller and demagnetizing current gains. The remainder of this paper is as follows. Section 2 provides an insight on the operation of the doubly fed induction generator in case of symmetrical voltage sips. Section 3 explains the crowbar approach, as well as the linear quadratic regulator approach, of DFIG control. Further, a clear explanation and subsequent flowchart of the African vultures optimization algorithm is provided. Section 4 provides the results of crowbar optimization using PSO and AVOA. Section 5 gives the results of the LQR, optimized using AVOA. Section 6 concludes the work conducted in this research

3. Control of the Doubly Fed Induction Generator

Under stead-state conditions, the operation of the DFIG is governed by the following equations [27,28]:

$$\vec{v_s} = R_s \vec{i_s} + \frac{d\vec{\varnothing_s}}{dt} \tag{1}$$

$$\vec{v_r} = R_r \vec{i_r} + \frac{d\vec{\varnothing_r}}{dt} - jw\vec{\varnothing_r} \tag{2}$$

$$\vec{\varnothing_s} = L_s \vec{i_s} + L_m \vec{i_r} \tag{3}$$

$$\vec{\varnothing_r} = L_r \vec{i_r} + L_m \vec{i_s} \tag{4}$$

where:

$\vec{v_s}$ and $\vec{v_r}$ are the stator and rotor voltage vectors, respectively;
$\vec{\varnothing_s}$ and $\vec{\varnothing_r}$ are the stator and rotor flux vectors, respectively;
$\vec{i_s}$ and $\vec{i_r}$ are the stator and rotor current vectors, respectively;
w is the rotor speed;

R_s and R_r are the stator and rotor resistances, respectively;
L_s, L_r and L_m are the stator, rotor, and magnetizing flux linkages, respectively.
From (3), making the rotor current the subject of the formula, the rotor flux can be expressed as [16,27]:

$$\vec{\varnothing_r} = \frac{L_m}{L_s}\vec{\varnothing_s} - \sigma L_r \vec{i_r} \tag{5}$$

where $\sigma = 1 - \frac{L_s}{L_m L_r}$. Substituting (5) into (2), the rotor voltage can then be expressed as [16,27,29]:

$$\vec{v_r} = \frac{L_m}{L_s}\left(\frac{d}{dt} - jw\right)\vec{\varnothing_s} + (R_r + \sigma L_r\left(\frac{d}{dt} - jw\right)\vec{i_r} \tag{6}$$

The first term in (6) denotes the rotor voltage induced due to the stator flux, when the rotor is open circuit. The second term corresponds to the voltage drop in the rotor resistance and rotor transient inductance. Considering that the stator voltage is a time variant measurement, the stator voltage vector can be represented as [16,27]:

$$\vec{v_s} = V_s e^{jw_s t} \tag{7}$$

where:
V_s is the peak magnitude of the stator voltage;
w_s is the synchronous speed of the revolving stator flux.
The stator flux can then be expressed as [16,27]:

$$\vec{\varnothing_s} = \frac{V_s e^{jw_s t}}{jw_s} \tag{8}$$

During the steady-state operation, the grid voltage is constant. Therefore, the stator flux is constant. The stator flux rotates at grid frequency and represents the forced response of the system. This is shown as [16,27]:

$$\vec{\varnothing_{sf}} = \frac{V_s e^{jw_s t}}{jw_s} \tag{9}$$

where $\vec{\varnothing_{sf}}$ denotes the forced flux. The rotor voltage due to the stator flux can be expressed as [16]:

$$\vec{v_{r0}} = jw_r \frac{L_m}{L_s}\varnothing_s = \frac{L_m}{L_s}\frac{w_r}{w_s}\frac{V_s e^{jw_s t}}{jw_s} \tag{10}$$

where:
$\vec{v_{r0}}$ is the rotor voltage due to the stator flux;
w_r is the slip speed.
Finally, the magnitude of the rotor voltage is [27,30]:

$$V_{r0} = V_s \frac{L_m}{L_s} s \tag{11}$$

With $s = \frac{w_r}{w_s}$. During the case of a partial symmetrical voltage dip, the stator voltage may be expressed as [30,31]:

$$\vec{v^s_s} = \begin{cases} V_s e^{jw_s t}, & |t < 0 \\ V_s e^{jw_s t}(1-k), & |t \geq 0 \end{cases} \tag{12}$$

where k represents the depth of the symmetrical fault. The stator flux can then be expressed as [16,29]:

$$\vec{\varnothing^s_s} = \begin{cases} \frac{\vec{v_s}}{jws} e^{jw_s t}, & |t < 0 \\ \frac{\vec{v_s}(1-k)}{jws} e^{jw_s t}, & |t \geq 0 \end{cases} \tag{13}$$

Because the stator flux is a state variable, the magnitude of the flux cannot change instantaneously. Instead, there is a gradual decay from one steady-state magnitude to another. The change in stator flux is seen as [27]:

$$\frac{d}{dt}\vec{\varnothing^s}_s = \vec{v^s}_s - \frac{R_s}{L_s}\vec{\varnothing^s}_s \tag{14}$$

During a three-phase symmetrical voltage dip, the stator flux comprises two components: the forced flux and the natural flux. These are quantized as [16,29]:

$$\vec{\varnothing^s}_{sf} = \frac{V_f e^{jw_s t}}{jw_s} \tag{15}$$

$$\vec{\varnothing^s}_{sn} = \frac{V_f e^{-t/\tau}}{jw_s} \tag{16}$$

where:

$\vec{\varnothing^s}_{sn}$ represents the natural stator flux;

V_f represents the post-fault stator voltage;

τ is a time constant which depends on the machine stator parameters.

During the dip, the forced flux continues to rotate at grid frequency, while the natural flux remains stationary with respect to the stator. In reference [15], the evolution of the stator flux during the case of a symmetrical voltage dip was provided. As evident, the flux continued to rotate in a circular fashion. This is owing to the effect of the forced flux, which was still rotating at synchronous speed. However, the circular trajectory of the flux was not perfectly centered. This is because of the natural flux. The flux continued to move in a decreasing spiral fashion, eventually becoming centered and subsequently reaching a new stead-state magnitude. Both the forced and natural fluxes induced individual rotor voltages [28]:

$$\vec{e^r}_r = \vec{e^r}_{rf} + \vec{e^r}_{rn} \tag{17}$$

where:

$\vec{e^r}_r$ is the total induced rotor emf;

$\vec{e^r}_{rf}$ is the emf induced due to the forced flux;

$\vec{e^r}_{rn}$ is the emf induced due to the natural flux.

These quantities can be expressed as [27,30]:

$$\vec{e^r}_{rf} = \frac{sL_m}{L_s} V_f e^{jw_s t} \tag{18}$$

$$\vec{e^r}_{rn} = -\frac{L_m}{L_s} jw_m \varnothing_{n0} e^{-t/\tau} \tag{19}$$

$$\vec{e^r}_r = \frac{L_m}{L_s} V_s (s(1-p)e^{jw_r t} - (1-s)pe^{jw_m t} e^{-t/\tau} \tag{20}$$

The second term in (20) is of particular interest. Due to this term being dependent on the slip, depth of fault, and the rotor speed, this term has the potential to induce tremendously large rotor voltages.

4. Research Methodology

The aim of this section is to provide insight into the methods undertaken to execute this investigation. The section starts by explaining the concept of the crowbar protection of the DFIG. Then, information regarding the linear quadratic regulator is provided, with a graphical representation of the function block diagram to be implemented. Lastly, the necessary theory and subsequent flowchart of the African vultures optimization algorithm, which will be utilized in this research, is provided.

4.1. Crowbar Protection

In Section 3, the effect of a symmetrical voltage dip on the DFIG was examined. However, this was considering that the rotor was open circuit. When the rotor is closed during the presence of a voltage dip, the machine behaves differently. This forms the basis of the crowbar method of protection. Consider the following [15]:

$$\vec{v^s}_s = R_s\vec{i^s}_s + \frac{d}{dt}\vec{\varnothing^s}_{sn} = 0 \tag{21}$$

Expressing the stator current with respect to the rotor current yields [15]:

$$\vec{i^s}_s = \frac{\vec{\varnothing^s}_{sn}}{L_s} - \frac{L_m}{L_r}\vec{i^s}_r \tag{22}$$

Substituting (22) into (21), the rate of change of the natural stator flux can be quantized as [15]:

$$\frac{d}{dt}\vec{\varnothing^s}_{sn} = -\frac{R_s}{L_s}\vec{\varnothing^s}_{sn} + \frac{L_m}{L_s}R_s\vec{i^s}_r \tag{23}$$

The second term in (23) depicts the influence of the rotor current on the evolution of the natural flux. This forms the basis of the crowbar method of control. In the case of a three-phase symmetrical voltage dip, the crowbar creates a short-circuit on the rotor of the machine, causing a large rotor current. This expedites the damping of the natural flux, as shown in Figures 4 and 5. From these figures, it is evident that a short circuit on the rotor terminals drastically reduces the damping time of the natural stator flux. Further, the short-circuit is effective at preventing a transient in the stator flux [15].

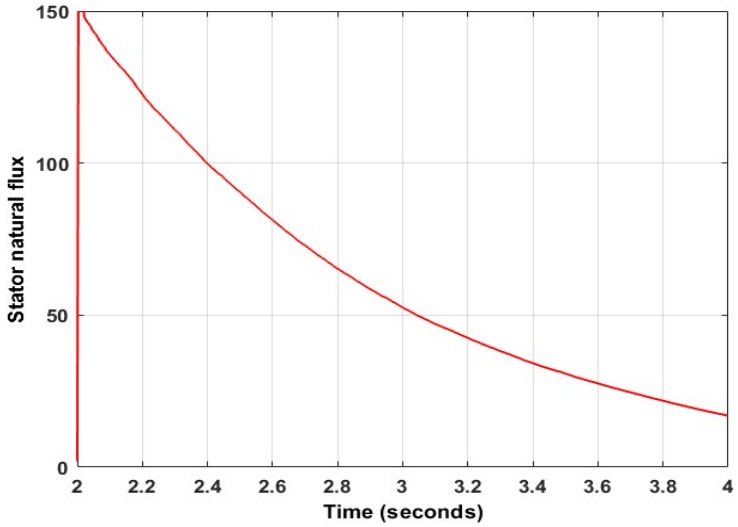

Figure 4. Stator natural flux for open-circuit rotor terminals.

Hence, it is concluded that the crowbar is an effective and ultimately essential method of protection of the DFIG. The crowbar resistors are open circuited during normal operation of the DFIG and are activated via power electronic switches during fault conditions. The topology of the crowbar circuit can be observed in Figure 6 [15].

4.2. The Linear Quadratic Regulator

The linear quadratic regulator is based on the specific linear time invariant system equation, which is given by [24,25]:

$$\dot{x} = Ax + Bu \tag{24}$$

$$y = Cx + Du \tag{25}$$

where:

$\dot{x}$ is the state of the system;
u is the system input;
y is the system output.

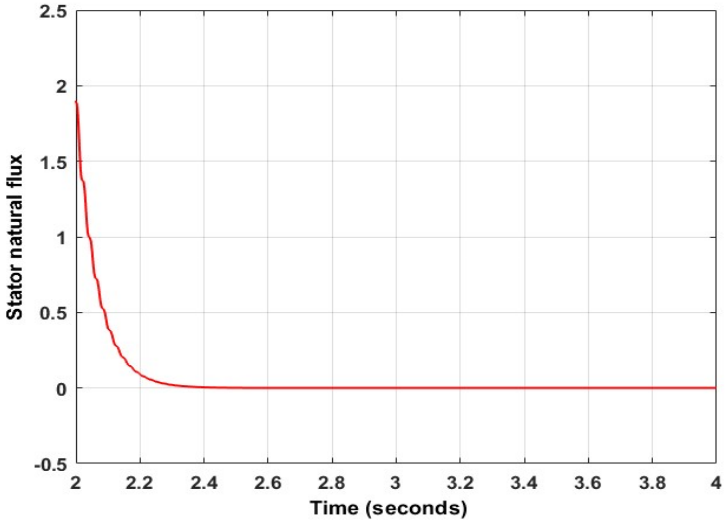

Figure 5. Stator natural flux for short-circuit rotor terminals.

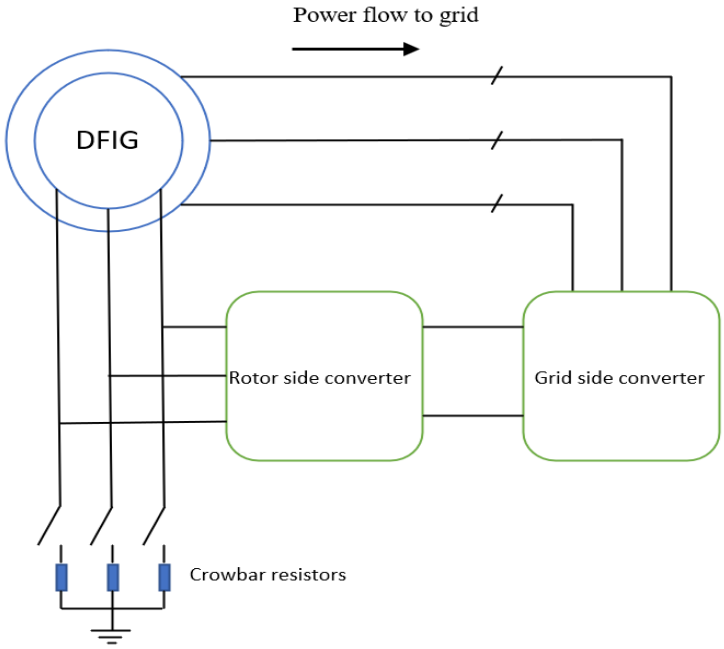

Figure 6. Topology of crowbar protection of DFIG [12].

The purpose of the LQR is to obtain an optimized gain, K, to satisfy the following [24,25]:

$$u(t) = -Kx(t) \tag{26}$$

This optimal value is generally obtained via the use of the following cost function [23–25]:

$$J(u) = \int_0^\infty [x^{-T}(t)Qx(t) + u^T(t)Ru(t)] \tag{27}$$

where Q and R are symmetrical matrices, used to weight the effort of control, and controller accuracy, respectively. Considering the stator-flux oriented vector control of the DFIG, the rotor voltages are expressed as [32,33]:

$$V_{dr} = R_r i_{dr} + \sigma L_r \frac{di_{dr}}{dt} - w_r \sigma L_r i_{qr} + \frac{L_m}{L_s} \frac{d\theta_{ds}}{dt} \tag{28}$$

$$V_{qr} = R_r i_{qr} + \sigma L_r \frac{di_{qr}}{dt} + w_r \sigma L_r i_{dr} + \frac{L_m}{L_s} \varnothing_{ds} \tag{29}$$

Therefore, the dynamic closed-loop behavior of the DFIG can be represented as [23,32]:

$$\dot{x} = Ax + Bu + Tr \tag{30}$$

$$\dot{y} = Cx \tag{31}$$

where:

$A, B, C,$ and T are square matrices;

r is the nonlinear measurable term.

Rewriting (28) and (29), making the derivative of the rotor current the output, the following is obtained [23,32]:

$$\begin{bmatrix} \frac{di_{dr}}{dt} \\ \frac{di_{qr}}{dt} \end{bmatrix} = \begin{bmatrix} \frac{-R_r}{\sigma L_r} & w_r \\ -w_r & \frac{-R_r}{\sigma L_r} \end{bmatrix} \begin{bmatrix} i_{dr} \\ i_{qr} \end{bmatrix} + \begin{bmatrix} \frac{1}{\sigma L_r} & 0 \\ 0 & \frac{1}{\sigma L_r} \end{bmatrix} \begin{bmatrix} v_{dr} \\ v_{qr} \end{bmatrix} + \begin{bmatrix} 0 & \frac{w_r L_m}{\sigma L_r L_s} \\ \frac{-w_r L_m}{\sigma L_r L_s} & 0 \end{bmatrix} \begin{bmatrix} \varnothing_s \\ 0 \end{bmatrix} \tag{32}$$

Generally, the linear quadratic regulator is not well suited for reference tracking applications. This may prove to be problematic, as the operation of the DFIG relies on the decoupled control of the rotor current magnitudes, which follow a reference value. To solve this, an integrator is added to the topology of the regulator. The function block diagram of the linear quadratic regulator to be applied to the DFIG is shown in Figure 7 [23].

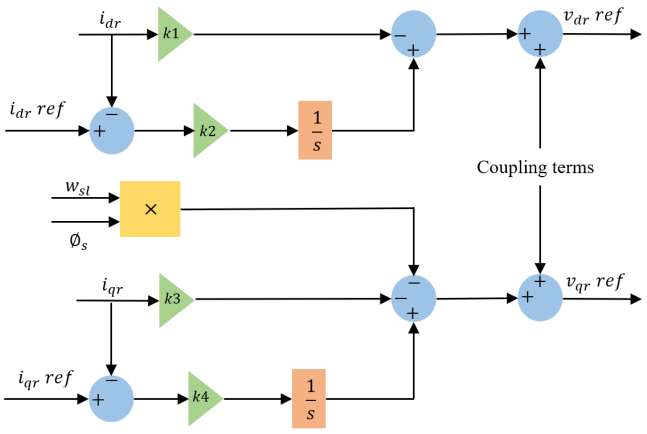

Figure 7. Functional block diagram of LQR applied to DFIG [20].

4.3. African Vultures Optimization Algorithm

The African vultures optimization algorithm is a recently developed swarm intelligence optimization technique. Inspired by the various African vulture species, this algorithm aims to mathematically model the scavenging behavior of these elusive birds. The algorithm is split into five distinct phases. In the first phase, the total number of vultures are split into two groups. Initially, each vulture is assigned a random position within the search space. Then, the fitness value of each vulture is computed. The vulture with the best fitness is placed in group one, whereas the vulture with the second-best fitness

is assigned group two. Thereafter, each of the remaining vultures are either sorted into group 1 or 2, depending on the following [26,34–36]:

$$R_i = \begin{cases} BV_1, if\ p_i = x_1 \\ BV_2,\ if\ p_i = x_2 \end{cases} \quad (33)$$

where:

BV_1 and BV_2 denote the groups of the best and second-best vultures, respectively;

x_1 and x_2 are random number in the domain [0,1], and whose total sum equal one; p_i is the probability based on the fitness function of the vulture being considered, as well as the fitness of the entire group. Its value is calculated based on the roulette wheel selection.

Note that there exists a large probability that p_i will not exactly be in value to x_1 or x_2. In such instance, the vulture will move to group where p_i is the closest to x. In the second phase, the starvation rate and the subsequent effect of satiety on the behavior of the vulture is considered. The hunger intensity of a particular vulture is expressed as [26,34–36]:

$$F_i = (2 \times r_1 +) \times z \times \left(1 - \frac{i}{max_i}\right) + t \quad (34)$$

$$t = h \times \left(sin^w\left(\frac{\pi}{2} \times \frac{i}{max_i}\right) + cos^w\left(\frac{\pi}{2} \times \frac{i}{max_i}\right) - 1\right) \quad (35)$$

where:

F_i is the satiation intensity of the ith vulture at the ith iteration;

r_1 is a random number in the domain [0,1];

z is a random number in the domain [−1,1];

i is the current iteration number;

max_i is the maximum number of iterations;

h is a random number in the domain [−2,2];

w is a predefined constant.

As evident in Equations (34) and (35), as the iteration magnitude progresses, the value of the satiation intensity decreases. The algorithm proposes that when the magnitude of F_i is greater than 1, the vultures can be assumed to have sufficient energy to explore different areas of food sources. However, when the magnitude of F_i is less than 1, the vultures are assumed to be low on energy, and therefore deploy exploitation in their current vicinity. The nature of the vultures' flight enables a high visibility of the ground below them. However, being cautious creatures, they spend most of their energy ensuring that areas with a potential food source are safe to exploit. The exploration of potential food sources of the African vulture is achieved via two methods. These are defined as [26,34–36]:

$$P_{i+1} = R_i - D_i \times F_i \quad (36)$$

$$P_{i+1} = R_i - F_i + r_2 \times ((u - l) \times r_3 + l) \quad (37)$$

where:

P_{i+1} is the next position of the ith vulture;

R_i is the position of one of the two best vultures;

r_2 and r_3 are randomized numbers in the range [0,1];

u and l are the upper and lower bounds of the search space, respectively;

D_i is the distance between the vulture in question and the current optimally situated vulture, and is denoted as [26,34–36]:

$$D_i = |X \times R_i - P_i| \quad (38)$$

where:

X is a random number in the domain [0,2];

P_i is the current position of the ith vulture.

The method of exploration chosen is dependent on a predefined constant, P_1. The value of P_1 lies in the domain [0,1]. Thereafter, a random number, also in the domain [0,1] is generated. If the value of P_1 is greater than that of the randomly generated number, Equation (36) is utilized. Otherwise, Equation (37) is deployed for exploration. As discussed earlier, if the magnitude of F_i is less than 1, the vulture enters the exploitation stage of food search. The exploitation phase comprises of two sub-phases. The first phase is executed as soon as F_i is less than 1. In this phase, as with the exploration phase, two possible exploitation methods exist. These are [26,34–36]:

$$P_{i+1} = D_i \times (F_i + r_4) - d_i \tag{39}$$

$$P_{i+1} = R_i - (K_1 + K_2) \tag{40}$$

$$d_i = R_i - P_i \tag{41}$$

$$K_1 = R_i \times \left(\frac{r_5 - P_i}{2\pi} \right) \times \cos(P_i) \tag{42}$$

$$K_1 = R_i \times \left(\frac{r_6 - P_i}{2\pi} \right) \times \cos(P_i) \tag{43}$$

where r_5 and r_6 are random numbers in the domain [0,1]. As with the exploration phase, the method of exploitation chosen is dependent on a predefined constant, P_2. The value of P_2 lies in the domain [0,1]. Thereafter, a random number, also in the domain [0,1], is generated. If the value of P_2 is greater than that of the randomly generated number, Equation (39) is utilized. Otherwise, Equation (40) is deployed for exploitation. The second phase of exploitation occurs when the magnitude of F_i is less than 0.5. As with exploration and phase one of exploitation, two possible scenarios exist. First, the fierce competition between vultures for a food source is mathematically modelled. The second scenario expresses the scavenging behavior of the vultures. In such an instance, the remaining vultures move to the position of the best vulture, to salvage the remaining food. These are expressed in Equations (44) and (47) and are as [26,34–36]:

$$P_{i+1} = \frac{T_1 + T_2}{2} \tag{44}$$

$$T_1 = BV_{1(i)} - \frac{BV_{1(i)} \times P_i}{BV_{1(i)} - P_i^2} \times F_i \tag{45}$$

$$T_2 = BV_{2(i)} - \frac{BV_{2(i)} \times P_i}{BV_{2(i)} - P_i^2} \times F_i \tag{46}$$

$$P_{i+1} = R_i - |d_i| \times F_i \times Levy(d) \tag{47}$$

where $Levy(d)$ denotes the conventional levy flight mechanism. As with the exploration phase, the method of exploitation chosen is dependent on a predefined constant, P_3. The value of P_3 lies in the domain [0,1]. Thereafter, a random number, also in the domain [0,1], is generated. If the value of P_3 is greater than that of the randomly generated number, Equation (44) is utilized. Otherwise, Equation (47) is deployed for exploitation. The flowchart depicting the process of execution of the AVOA is shown in Figure 8 [26,34–36].

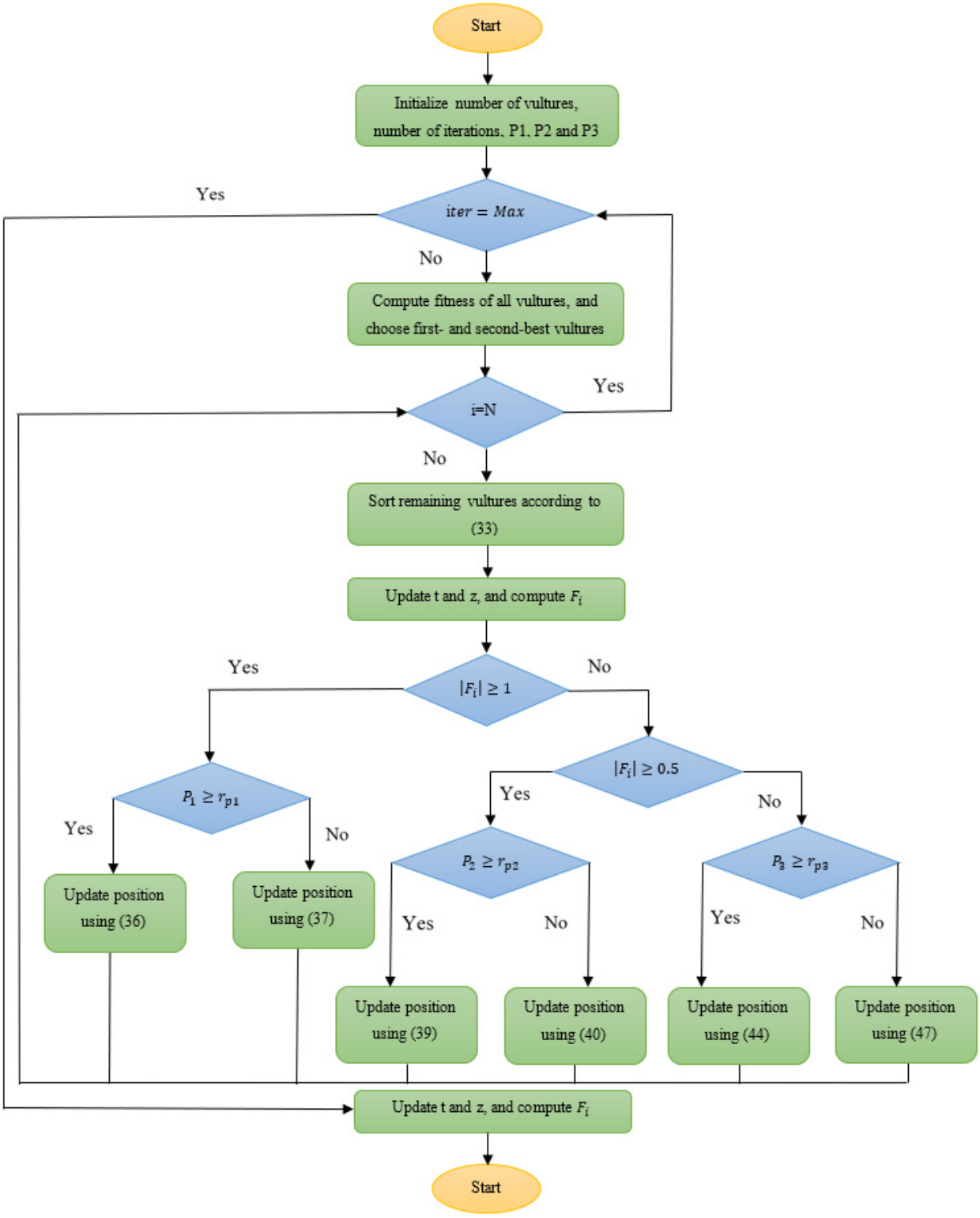

Figure 8. Method of execution of AVOA [30–33].

5. Investigation into Optimization of Crowbar Resistance via Swarm Intelligence

The aim of this section is the investigate the effectiveness of utilizing the swarm intelligence for determining the optimal setting of the crowbar resistance values. It is known that a high crowbar resistance will limit the fault current, but at the expense of a significantly higher DC voltage. Similarly, a smaller resistance will limit the DC voltage, but will produce an exorbitantly high fault current transient. Both scenarios produce

unfavorable outcomes. The aim of the optimal crowbar setting is to attempt to provide a viable trade-off between the rotor transient current and the DC voltage magnitudes. For this purpose, the well-known particle swarm optimization and the recently proposed African vultures optimization algorithm will be implemented. The results for both PSO and AVOA for a 70%, 80%, and 90% symmetrical voltage dip are presented. The results are in terms of rotor current and DC voltage transient and settling times. Each of the utilized optimization techniques were subject to 20 iterations with 20 search agents. The lower and upper bounds of the search space were set to 0.00001 and 10, respectively.

5.1. Case 1a: Voltage Dip of 70%

Figures 9–12 depict the results of applying swarm intelligence to the optimization of crowbar resistance for a 70% dip. Figures 9 and 10 show the rotor current and DC voltage magnitudes, respectively, when applying PSO. Figures 11 and 12 show the rotor current and DC voltage magnitudes, respectively, when applying AVOA.

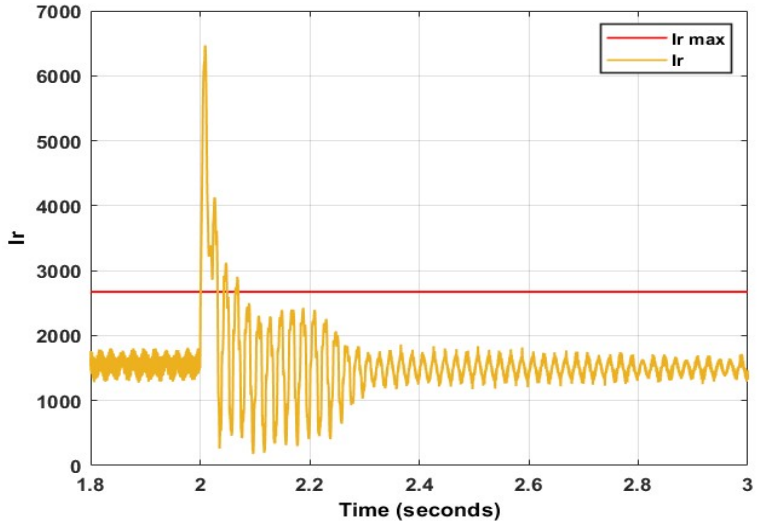

Figure 9. Rotor current transient using PSO at 70% dip.

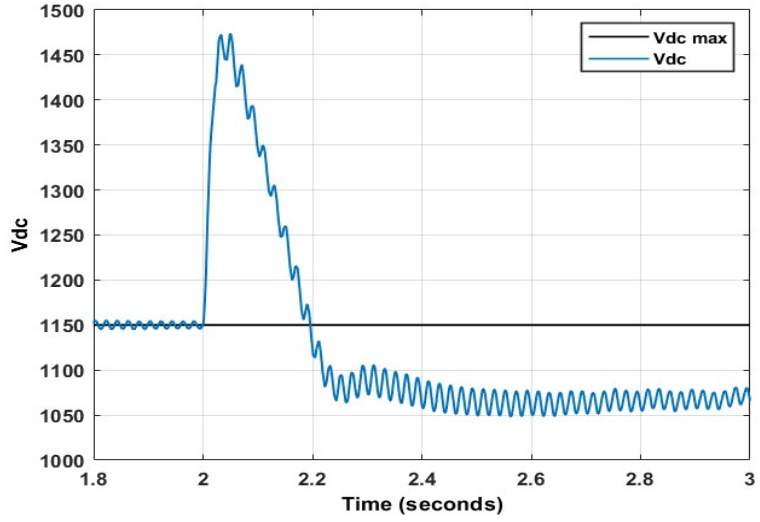

Figure 10. DC voltage transient using PSO at 70% dip.

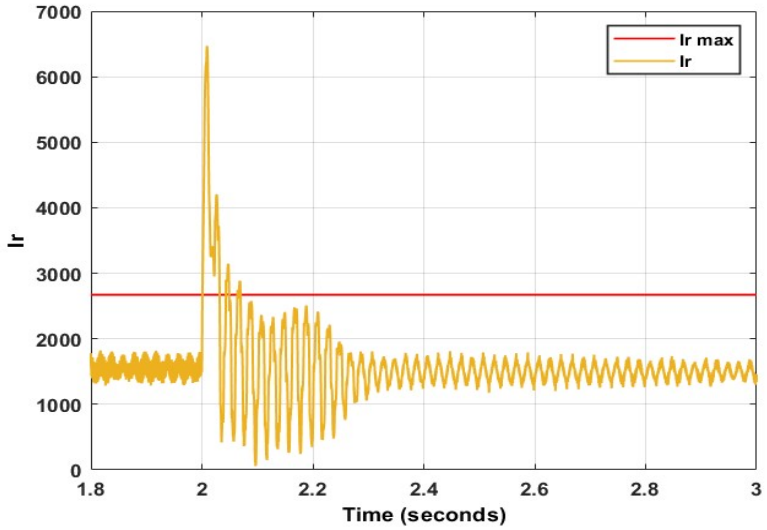

Figure 11. Rotor current transient using AVOA at 70% dip.

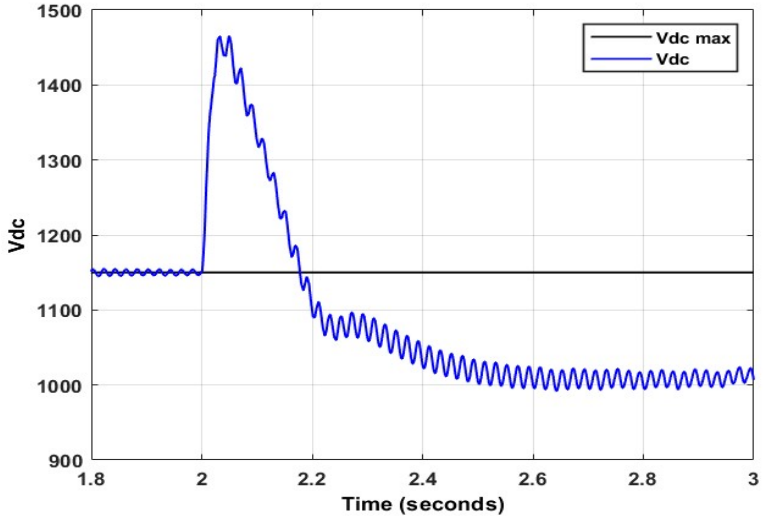

Figure 12. DC voltage transient using AVOA at 70% dip.

From Figure 9, it is observed that the transient rotor current when applying PSO is 6468 A, with a settling time of 70 ms. Considering the DC voltage when utilizing PSO in Figure 10, the transient voltage is 1465 A. The settling time of this voltage is 175 ms. From Figure 11, it is observed that the transient rotor current when applying AVOA is 6472 A, with a settling time of 70 ms. Considering the DC voltage when utilizing PSO in Figure 12, the transient voltage is 1465 A. The settling time of this voltage is 175 ms. It is therefore noted that for a 70% voltage dip, both the algorithms produced identical transient DC voltages and settling times. However, PSO exhibited superiority over AVOA for the rotor current transient, by a minute factor of 0.062%.

5.2. Case 1b: Voltage Dip of 80%

Figures 13–16 depict the results of applying swarm intelligence to the optimization of crowbar resistance for an 80% dip. Figures 13 and 14 show the rotor current and DC voltage magnitudes, respectively, when applying PSO. Figures 15 and 16 show the rotor current and DC voltage magnitudes, respectively, when applying AVOA.

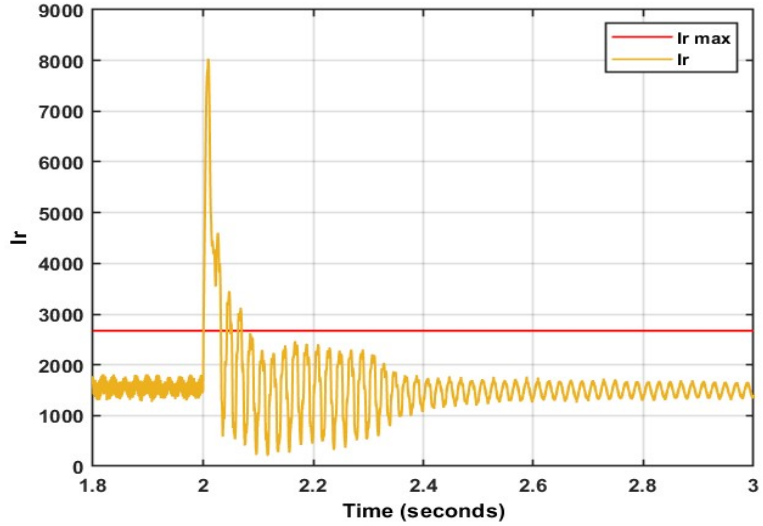

Figure 13. Rotor current transient using PSO at 80% dip.

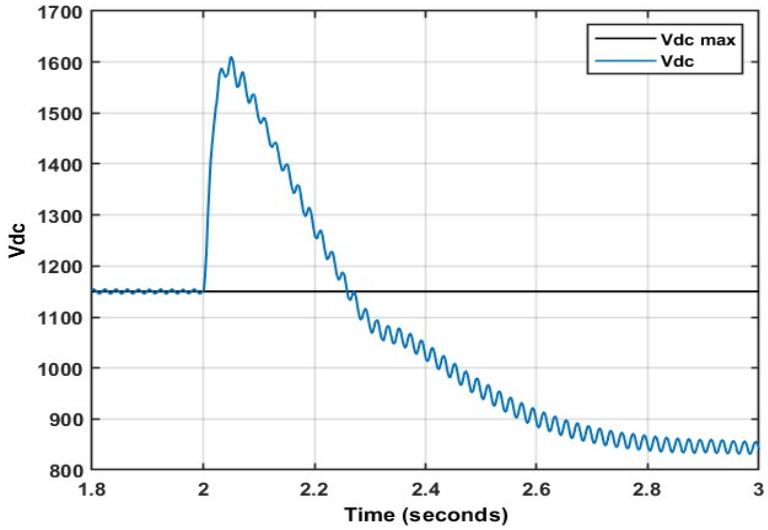

Figure 14. DC voltage transient using PSO at 80% dip.

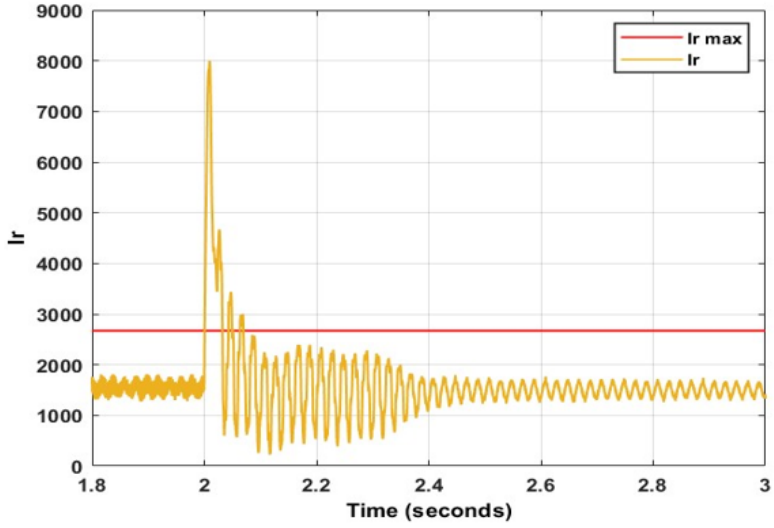

Figure 15. Rotor current transient using AVOA at 80% dip.

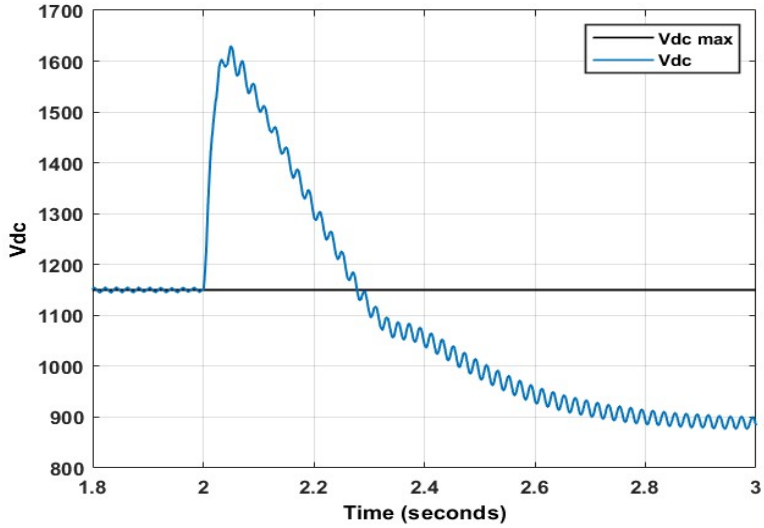

Figure 16. DC voltage transient using AVOA at 80% dip.

From Figure 13, it is observed that the transient rotor current when applying PSO is 8035 A, with a settling time of 70 ms. Considering the DC voltage when utilizing PSO in Figure 14, the transient voltage is 1612 A. The settling time of this voltage is 260 ms. From Figure 15, it is observed that the transient rotor current when applying AVOA is 7999 A, with a settling time of 70 ms. Considering the DC voltage when utilizing PSO in Figure 16, the transient voltage is 1630 A. The settling time of this voltage is 280 ms. It is therefore noted that for a 70% voltage dip, both the algorithms produced superior results, but in different aspects. PSO exhibited superiority with regards to the DC voltage transient and settling time, in the order of 1.12% and 7.69%, respectively. AVOA produced a superior rotor current transient by a magnitude of 0.45%.

5.3. Case 1c: Voltage Dip of 90%

Figures 17–20 depict the results of applying swarm intelligence to the optimization of crowbar resistance for a 90% dip. Figures 17 and 18 show the rotor current and DC voltage magnitudes, respectively, when applying PSO. Figures 19 and 20 show the rotor current and DC voltage magnitudes, respectively, when applying AVOA.

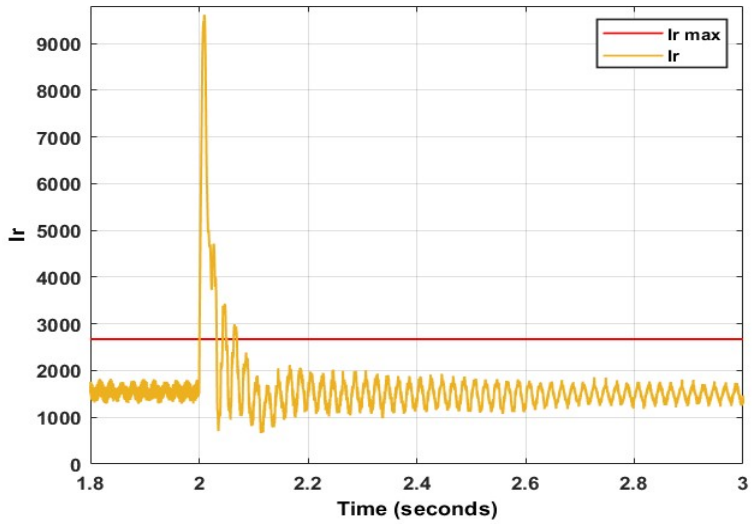

Figure 17. Rotor current transient using PSO at 90% dip.

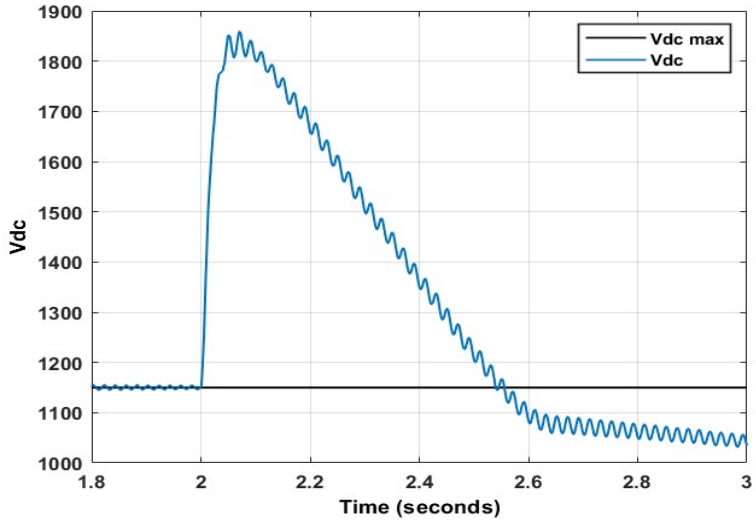

Figure 18. DC voltage transient using PSO at 90% dip.

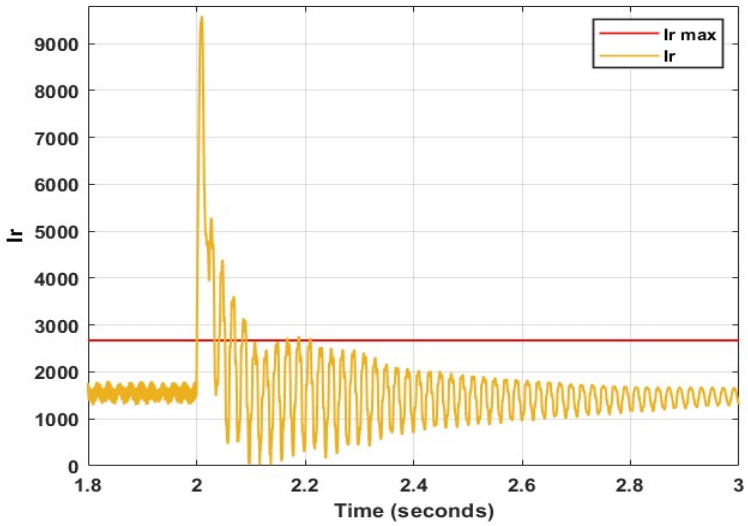

Figure 19. Rotor current transient using AVOA at 90% dip.

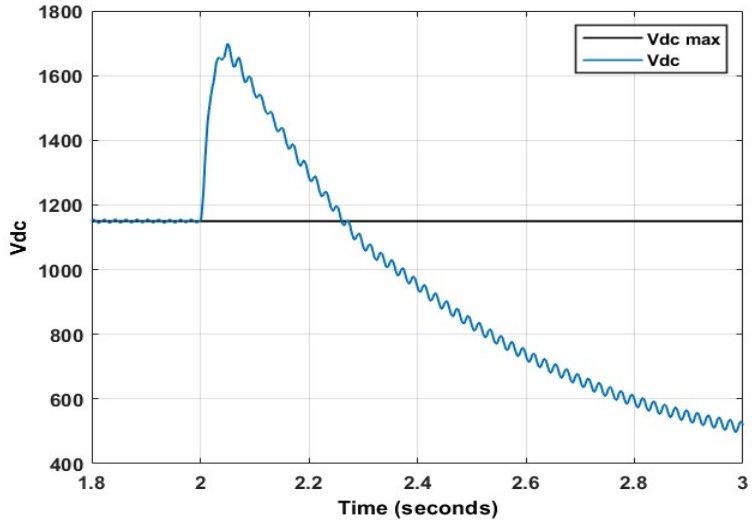

Figure 20. DC voltage transient using AVOA at 90% dip.

From Figure 17, it is observed that the transient rotor current when applying PSO is 9612 A, with a settling time of 70 ms. Considering the DC voltage when utilizing PSO in Figure 18, the transient voltage is 1860 A. The settling time of this voltage is 555 ms. From Figure 19, it is observed that the transient rotor current when applying AVOA is 9580 A, with a settling time of 70 ms. Considering the DC voltage when utilizing AVOA in Figure 20, the transient voltage is 1700 A. The settling time of this voltage is 275 ms. It is therefore noted that for a 70% voltage dip, the AVOA produced the best results. While the settling time of the rotor current was identical, the AVOA exhibited superiority with regards to the rotor current transient, DC voltage transient, and DC voltage settling time. This is in the order of 0.33%, 8.6%, and a massive 101.8%, respectively. The results of the experiments conducted are summarized in Table 1. From this, it can be concluded that for moderately severe symmetrical voltage dips, PSO is the preferred optimization technique. However, for voltage dips below 80%, the AVOA exhibits far more superior results.

Table 1. Summary of results for optimization of crowbar resistance using swarm intelligence.

		$I_{r(transient)}$ (A)	$t_{r\ (setling)}$ (ms)	$V_{dc(transient)}$ (A)	$t_{dc\ (setling)}$ (ms)
70%	PSO	**6468**	**70**	**1465**	**175**
	AVOA	6472	**70**	**1465**	**175**
80%	PSO	8035	**70**	**1612**	**260**
	AVOA	**7999**	**70**	1630	280
90%	PSO	9612	**70**	1860	555
	AVOA	**9580**	**70**	**1700**	**275**

6. Investigation into African Vultures Optimization Algorithm for the Optimization of the Linear Quadratic Regulator and Demagnetizing Current Injection Gains

As observed in Section 5, the crowbar protection scheme successfully provides protection to the DFIG. However, this requires the DFIG to be disconnected from the grid, and therefore is not compliant with modern grid codes. This section aims to analyze the results of the linear quadratic regulator and demagnetizing current injection (DCI) applied to the DFIG under symmetrical grid faults. To enhance the tracking capability of the LQR, an integrator is added to the control mechanism. The LQR and DCI controller gains were optimized using the African vultures optimization algorithm and compared to the conventional PI controller optimized via the well-known PSO. The choice of power converter utilized for switching was the two-level voltage source converter. Three voltages dips were considered: 70%, 80%, and 90%. The results were analyzed in terms of peak rotor current and DC voltage, as well as steady state ripple and steady-state error of the reactive-power controlling rotor current. During the fault, the amount of reactive power injected into the grid is increased, whereas the stator active power reference is set to zero. The steady-state error is evaluated for the last 0.3 s of the simulation. This is to allow the system sufficient time to dampen oscillations. The African vultures optimization algorithm was subject to 20 iterations of 20 search agents, with an upper and lower bound of 0 and 100, respectively, for the LQR gains, and 0 and 50, respectively, for the DCI controller gains.

6.1. Case 2a: Voltage Dip of 70%

Table 2 indicates the optimized gains for the PI controller, considering a voltage dip of 70%. Figures 21 and 22 represent the total rotor current magnitude and DC voltage, respectively, of the PI controller. Figures 23 and 24 indicate the rotor direct axis current steady state ripple and steady state error, respectively, of the PI controller. From Figure 21, the peak rotor current magnitude is observed to be at 6256 A, whereas Figure 22 depicts the peak DC voltage as 1634 V. The steady-state ripple of the rotor direct axis current, as shown in Figure 23, is 283 A, with the average steady state value in Figure 24 at 1409 A. This correlates to an error percentage of 6.07%

Table 2. PI controller gains for 70% dip.

$K_{p(idr)}$	$K_{i(idr)}$	$K_{p(iqr)}$	$K_{i(iir)}$
53.5253	91.1925	54.9872	48.5211

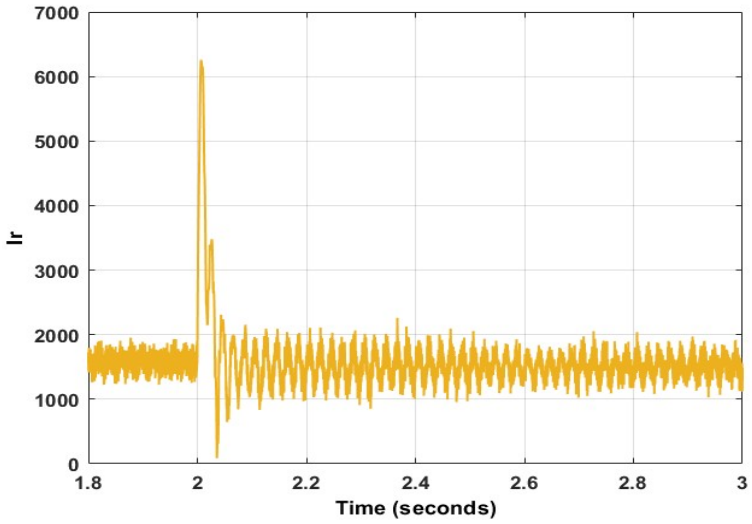

Figure 21. Rotor current transient using PI at 70% dip.

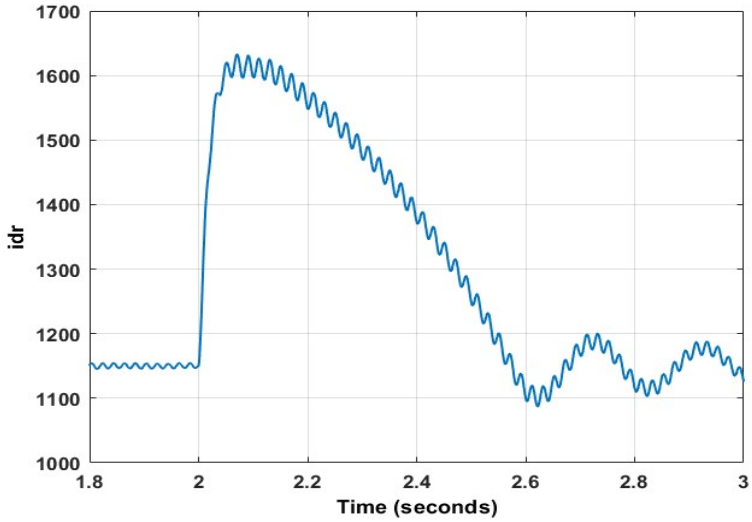

Figure 22. DC voltage transient using PI at 70% dip.

Table 3 indicates the optimized gains for the demagnetizing current injection (DCI), considering a voltage dip of 70%. Figures 25 and 26 represent the total rotor current magnitude and DC voltage, respectively, of the DCI. Figures 27 and 28 indicate the rotor direct axis current steady state ripple and steady state error, respectively, of the DCI. From Figure 25, the peak rotor current magnitude is observed to be 5557 A, indicating a superiority of 12.58% over the conventional PI controller. Figure 26 depicts the peak DC voltage as 1597 V, exhibiting a 2.32% better response than the PI controller. The steady-state ripple of the rotor direct axis current, as shown in Figure 27, is 379.5 A, which is 33.92% inferior to the PI controller. The average steady state value in Figure 28 is 1355.5 A. This correlates to an error percentage of 6.89%. This error is minorly inferior to the conventional PI controller.

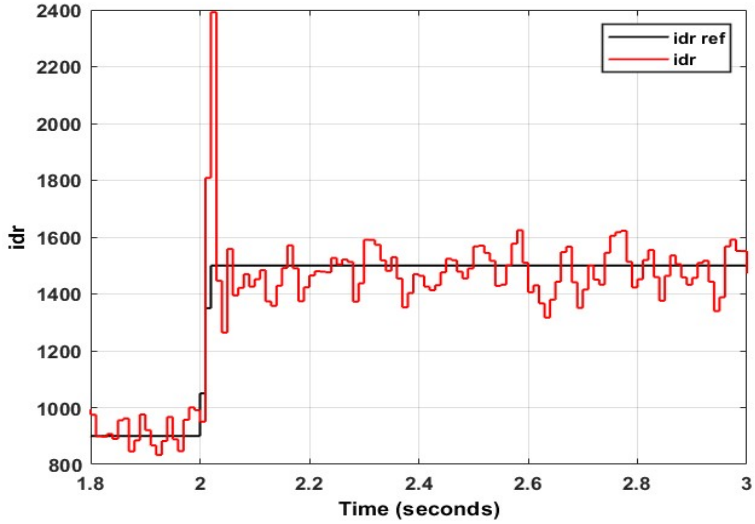

Figure 23. Rotor direct axis current ripple using PI at 70% dip.

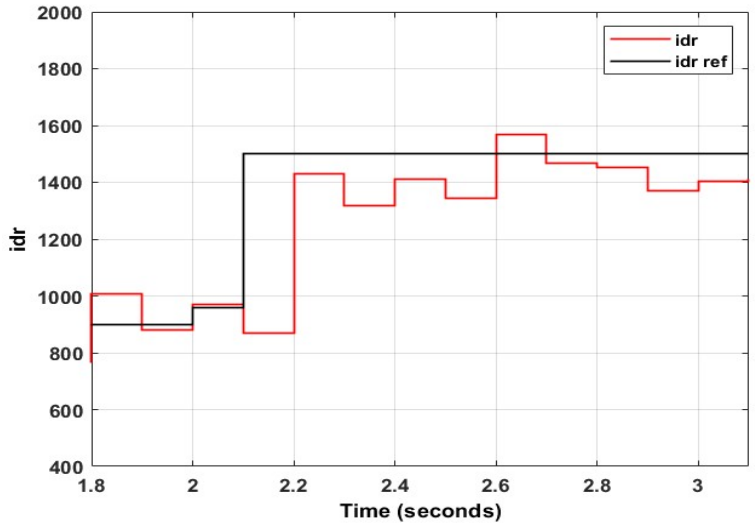

Figure 24. Rotor direct axis current average using PI at 70% dip.

Table 3. DCI controller gains at 70% dip.

K_1	K_2
49.2779	48.4913

Table 4 indicates the optimized gains for the LQR, considering a voltage dip of 70%. Figures 29 and 30 represent the total rotor current magnitude and DC voltage, respectively, of the LQR. Figures 31 and 32 indicate the rotor direct axis current steady state ripple and steady state error, respectively, of the LQR. From Figure 29, the peak rotor current magnitude is observed to be 3735 A, indicating a superiority of 67.5% over the conventional PI controller. Figure 30 depicts the peak DC voltage as 1377 V, exhibiting a 18.66% better response than the PI controller. The steady-state ripple of the rotor direct axis current, as shown in Figure 31, is 256.5 A, which is 10.33% superior to the PI controller. The average steady state value in Figure 32 is 1409 A. This correlates to an error percentage of 10.07%. This error is inferior to the conventional PI controller.

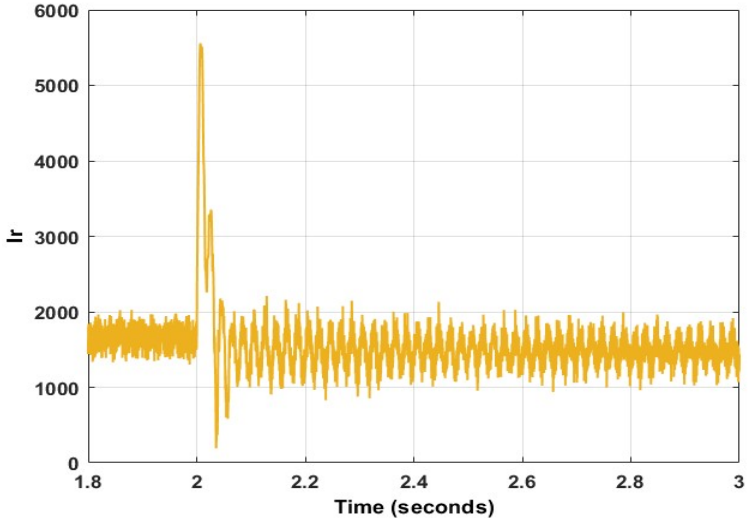

Figure 25. Rotor current transient using DCI at 70% dip.

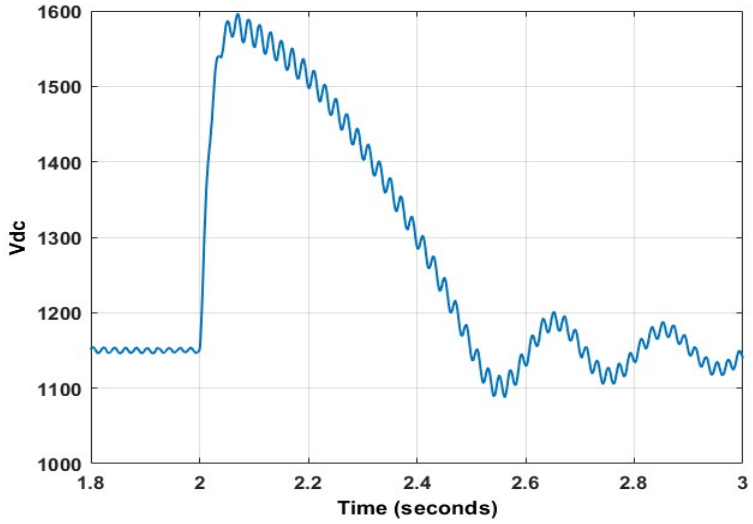

Figure 26. DC voltage transient using DCI at 70% dip.

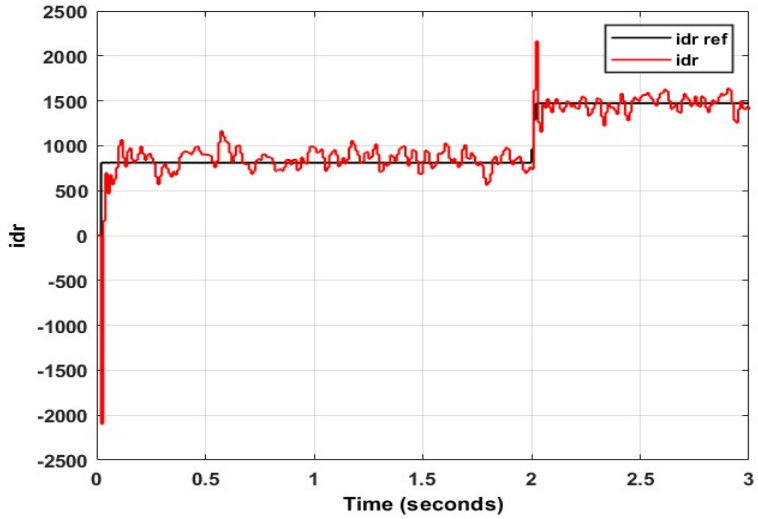

Figure 27. Rotor direct axis current ripple using DCI at 70% dip.

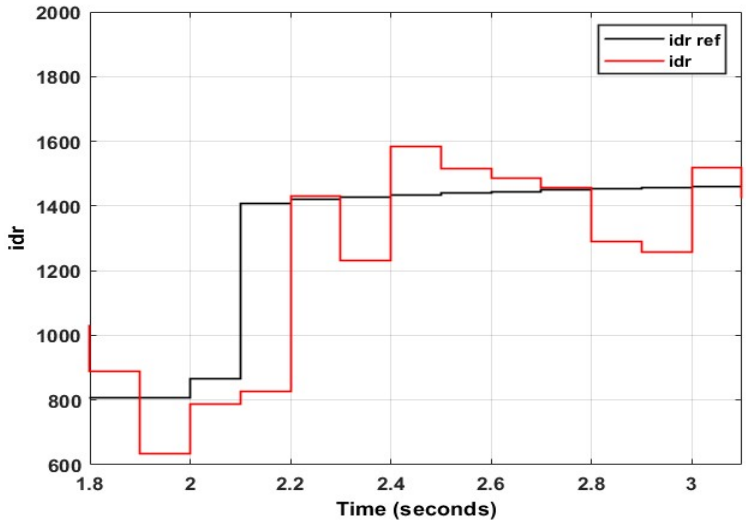

Figure 28. Rotor direct axis current average using DCI at 70% dip.

Table 4. LQR controller gains at 70% dip.

K_1	K_2	K_3	K_4
100	34.9938	51.29618	7.437115

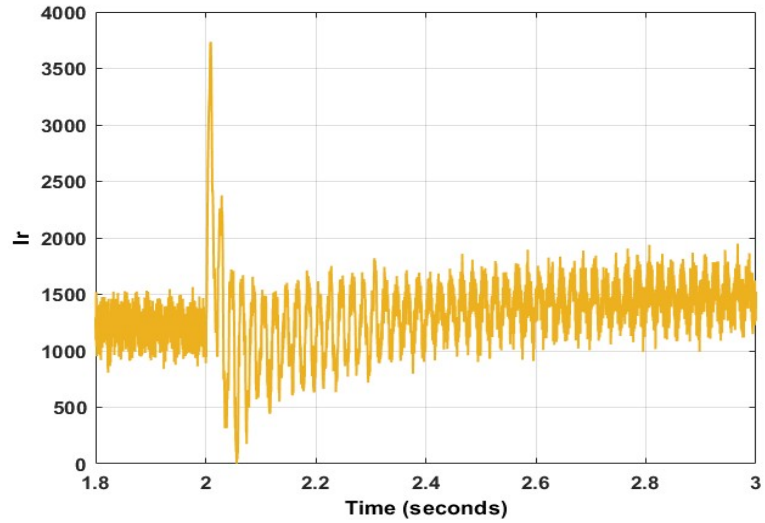

Figure 29. Rotor current transient using LQR at 70% dip.

6.2. Case 2b: Voltage Dip of 80%

Table 5 indicates the optimized gains for the PI controller, considering a voltage dip of 80%. Figures 33 and 34 represent the total rotor current magnitude and DC voltage, respectively, of the PI controller. Figures 35 and 36 indicate the rotor direct axis current steady state ripple and steady state error, respectively, of the PI controller. From Figure 33, the peak rotor current magnitude is observed to be 7550 A, whereas Figure 34 depicts the peak DC voltage as 1839 V. The steady-state ripple of the rotor direct axis current, as shown in Figure 35, is 456 A, with the average steady state value in Figure 36 at 1407 A. This correlates to an error percentage of 6.2%

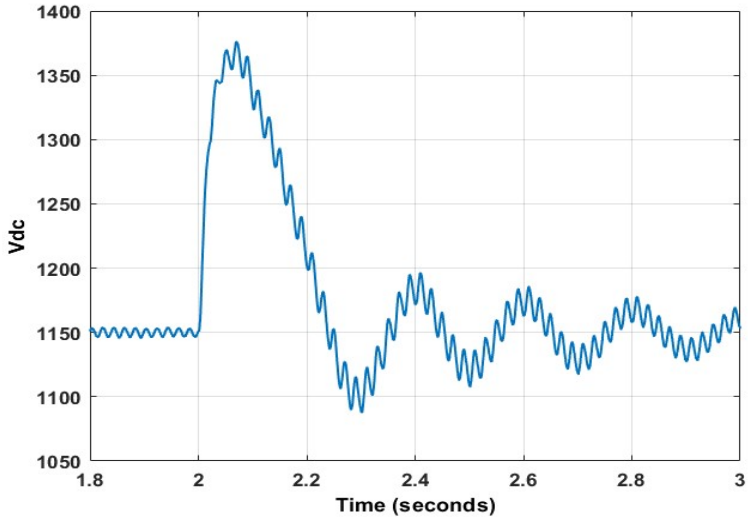

Figure 30. DC voltage transient using LQR at 70% dip.

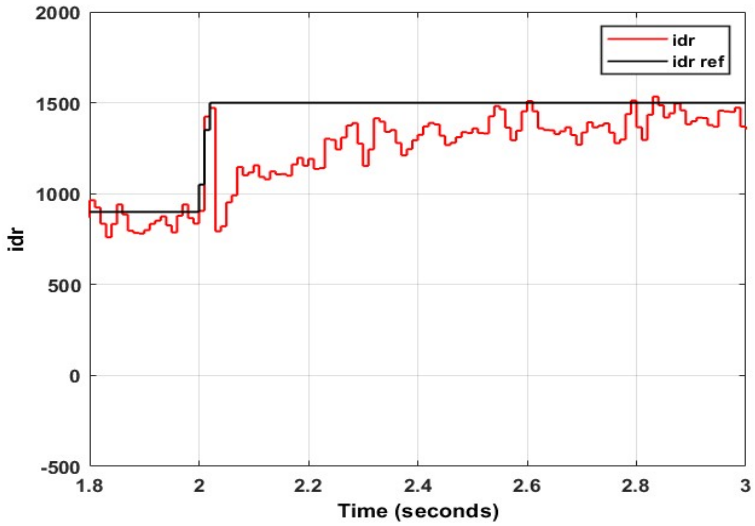

Figure 31. Rotor direct axis current ripple using LQR at 70% dip.

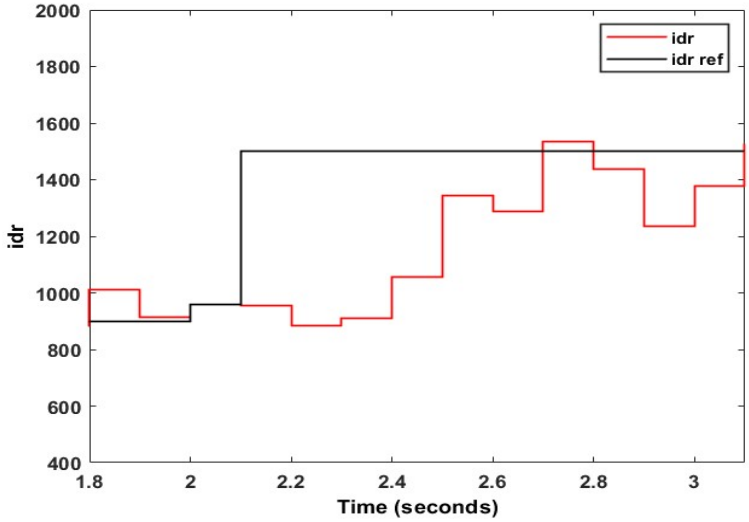

Figure 32. Rotor direct axis current average using LQR at 70% dip.

Table 5. PI controller gains for 80% dip.

$K_{p(idr)}$	$K_{i(idr)}$	$K_{p(iqr)}$	$K_{i(iir)}$
62.9078	0	65.535	12.8299

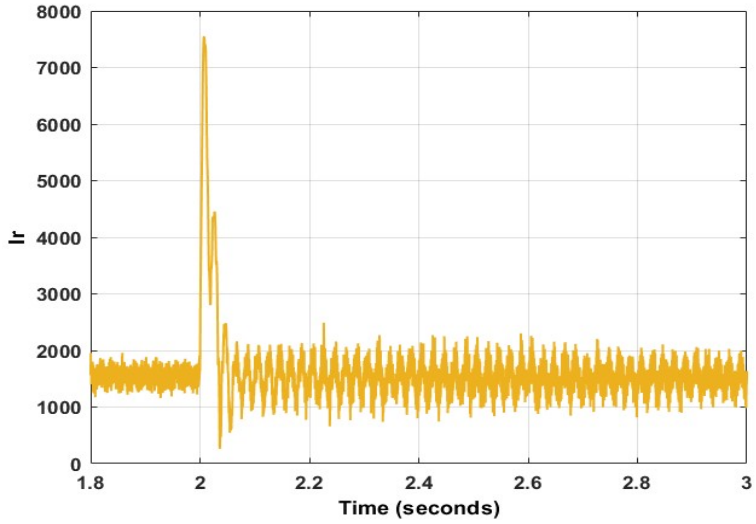

Figure 33. Rotor current transient using PI at 80% dip.

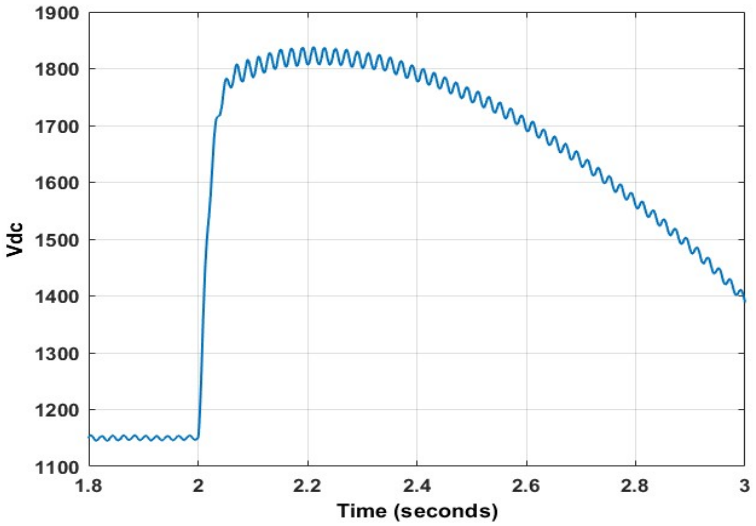

Figure 34. DC voltage transient using PI at 80% dip.

Table 6 indicates the optimized gains for the DCI, considering a voltage dip of 80%. Figures 37 and 38 represent the total rotor current magnitude and DC voltage, respectively, of the DCI. Figures 39 and 40 indicate the rotor direct axis current steady state ripple and steady state error, respectively, of the DCI. From Figure 37, the peak rotor current magnitude is observed to be 7325 A, indicating a superiority of 52.4% over the conventional PI controller. Figure 38 depicts the peak DC voltage as 1787 V, exhibiting a 20.35% better response than the PI controller. The steady-state ripple of the rotor direct axis current, as shown in Figure 39, is 357.5 A, which is 27.55% superior to the PI controller. The average steady state value in Figure 40 is 1173.67 A. This correlates to an error percentage of 19.74%. This error is superior to the conventional PI controller

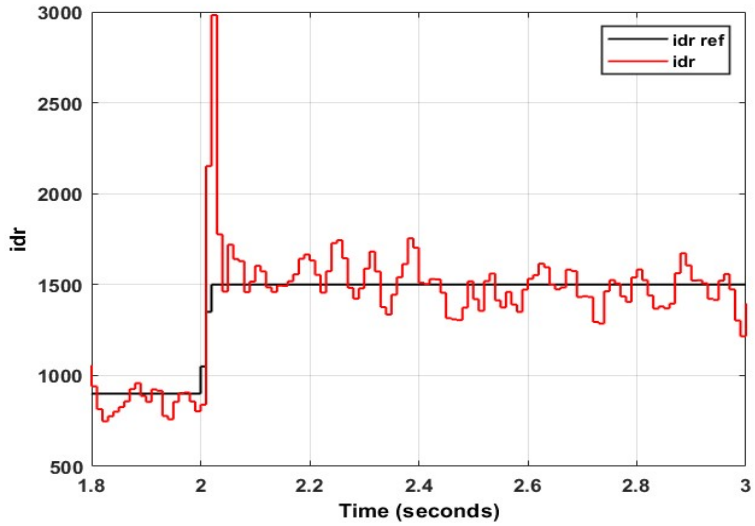

Figure 35. Rotor direct axis current ripple using PI at 80% dip.

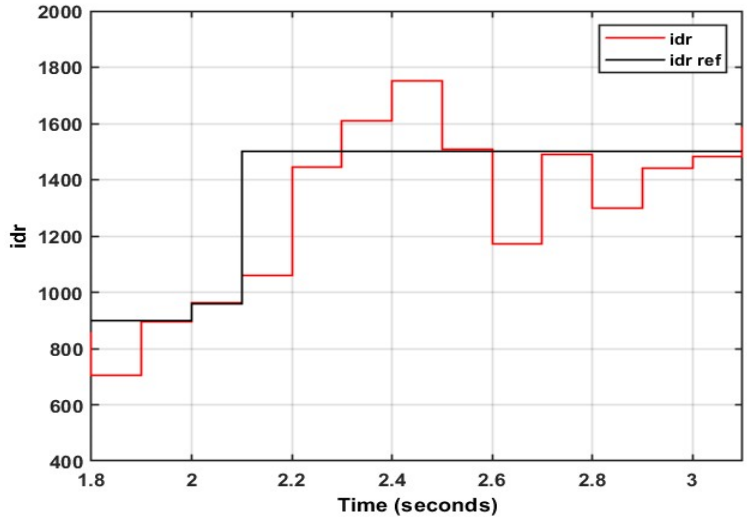

Figure 36. Rotor direct axis current average using PI at 80% dip.

Table 6. DCI controller gains at 80% dip.

K_1	K_2
49.9272	45.3424

Table 7 indicates the optimized gains for the LQR, considering a voltage dip of 80%. Figures 41 and 42 represent the total rotor current magnitude and DC voltage, respectively, of the LQR. Figures 43 and 44 indicate the rotor direct axis current steady state ripple and steady state error, respectively, of the LQR. From Figure 41, the peak rotor current magnitude is observed to be 4954 A, indicating a superiority of 52.4% over the conventional PI controller. Figure 42 depicts the peak DC voltage as 1528 V, exhibiting a 20.35% better response than the PI controller. The steady-state ripple of the rotor direct axis current, as shown in Figure 43, is 290 A, which is 57.24% superior to the PI controller. The average steady state value in Figure 44 is 1427 A. This correlates to an error percentage of 4.87%. This error is superior to the conventional PI controller, which can be attributed to the zero-gain value in Table 5, which was obtained for the PI controller.

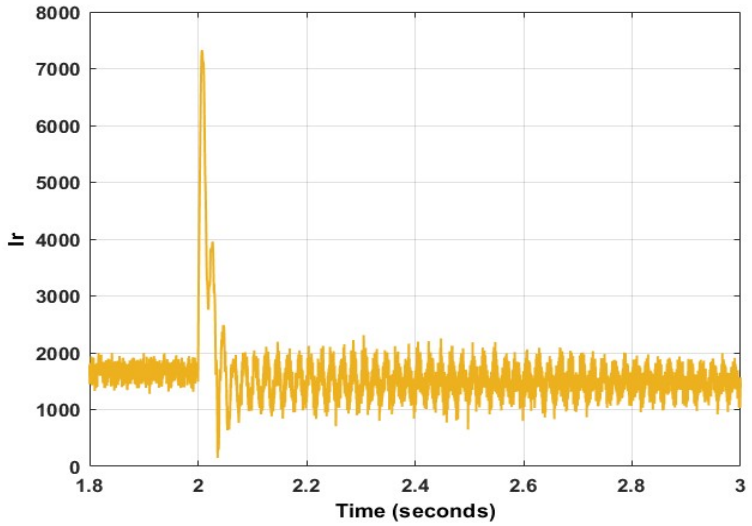

Figure 37. Rotor current transient using DCI at 80% dip.

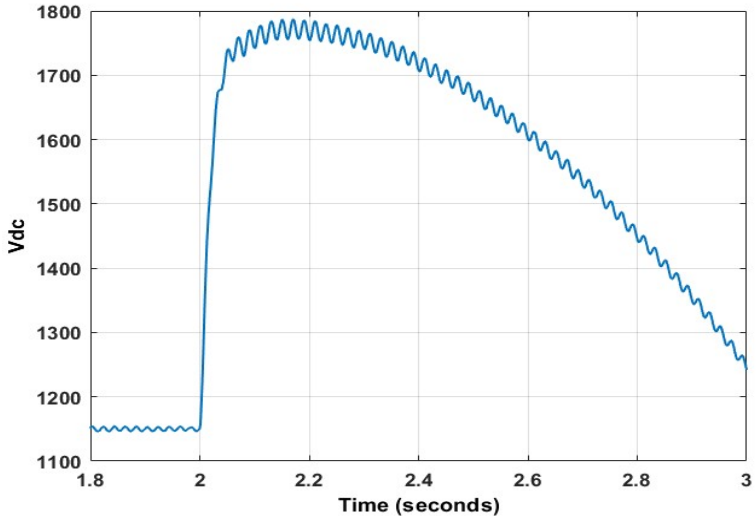

Figure 38. DC voltage transient using DCI at 80% dip.

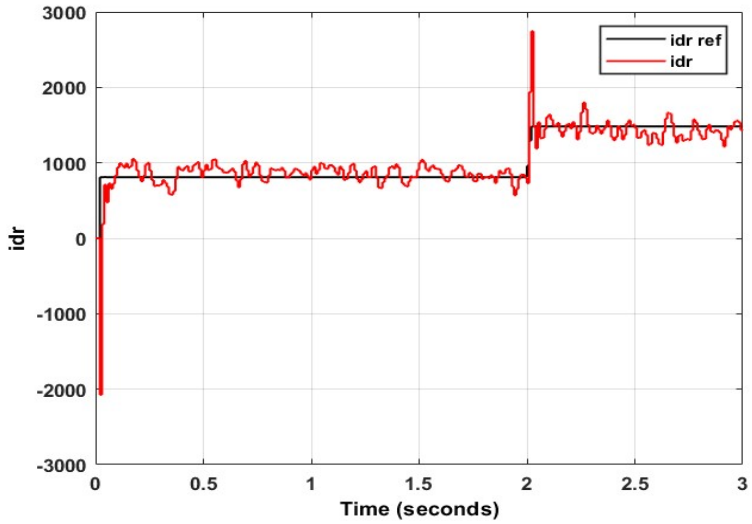

Figure 39. Rotor direct axis current ripple using DCI at 80% dip.

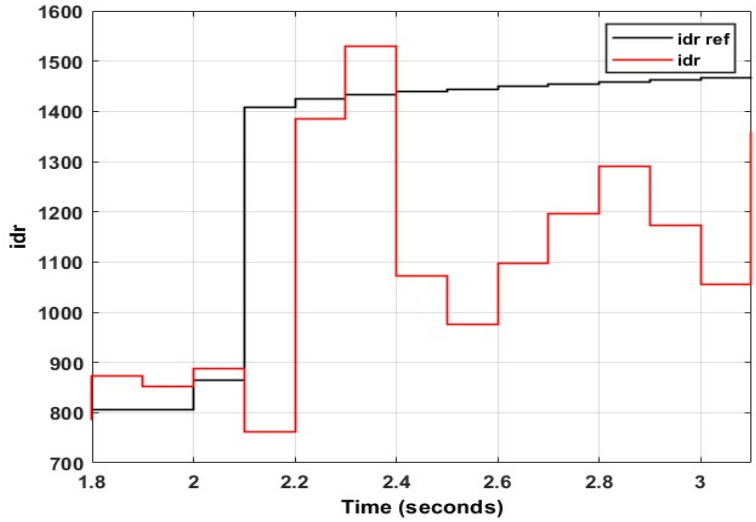

Figure 40. Rotor direct axis current average using DCI at 80% dip.

Table 7. LQR controller gains at 80% dip.

K_1	K_2	K_3	K_4
99.7437	37.8219	45.7003	6.71573

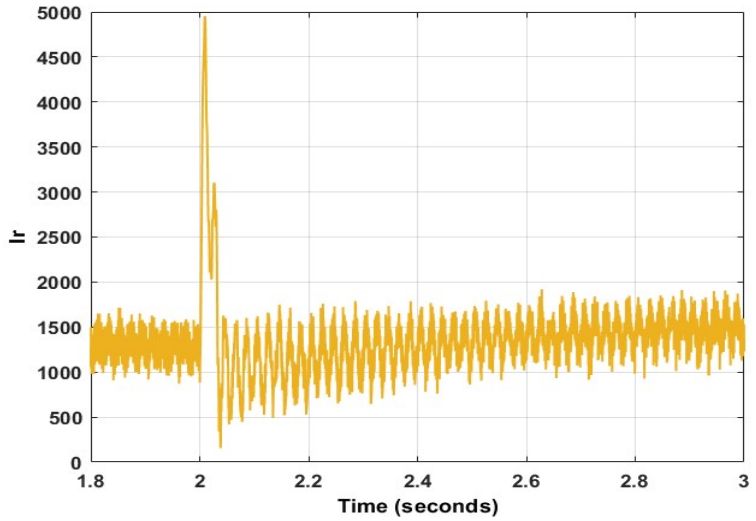

Figure 41. Rotor current transient using LQR at 80% dip.

6.3. Case 2c: Voltage Dip of 90%

Table 8 indicates the optimized gains for the PI controller, considering a voltage dip of 90%. Figures 45 and 46 represent the total rotor current magnitude and DC voltage, respectively, of the PI controller. Figures 47 and 48 indicate the rotor direct axis current steady state ripple and steady state error, respectively, of the PI controller. From Figure 45, the peak rotor current magnitude is observed to be 9110 A, whereas Figure 46 depicts the peak DC voltage as 2176 V. The steady-state ripple of the rotor direct axis current, as shown in Figure 47, is 416 A, with the average steady state value in Figure 48 at 1438 A. This correlates to an error percentage of 4.3%.

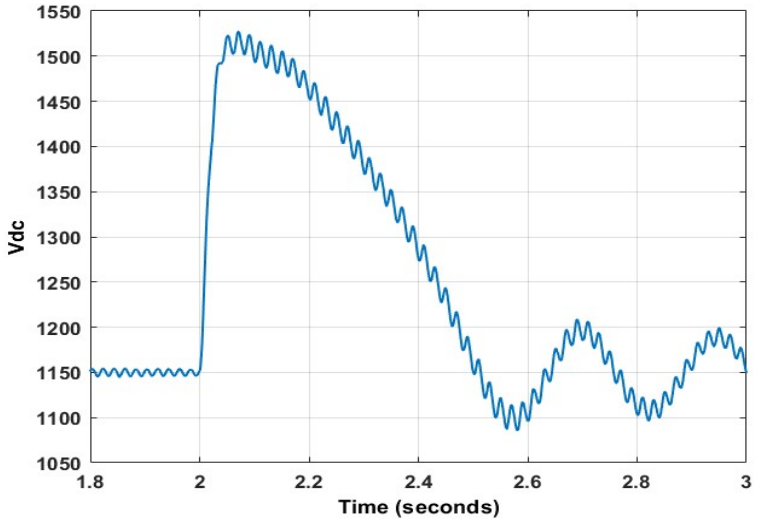

Figure 42. DC voltage transient using LQR at 80% dip.

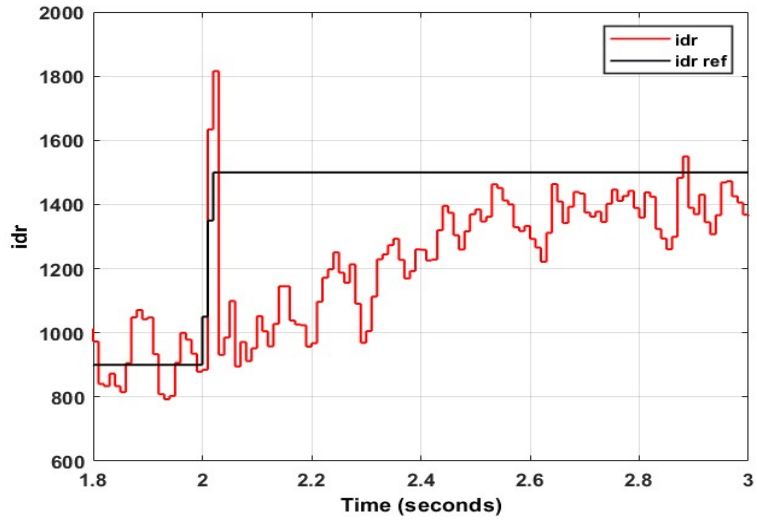

Figure 43. Rotor direct axis current ripple using LQR at 80% dip.

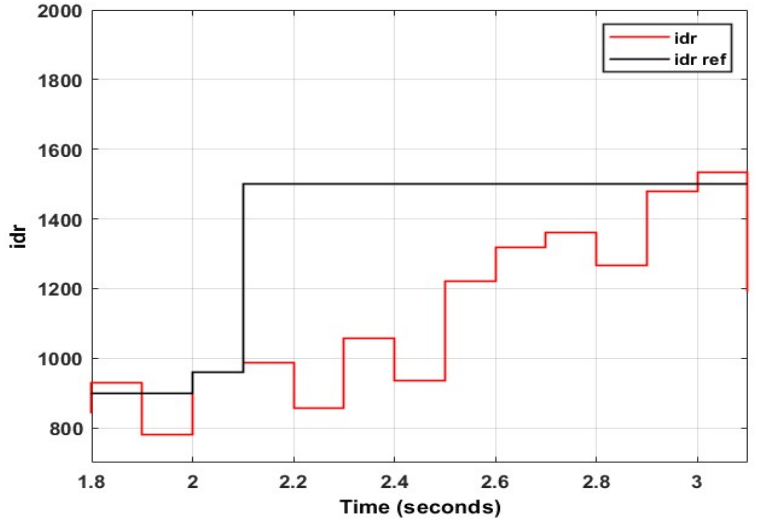

Figure 44. Rotor direct axis current average using LQR at 80% dip.

Table 8. PI controller gains at 90% dip.

$K_{p(idr)}$	$K_{i(idr)}$	$K_{p(iqr)}$	$K_{i(iir)}$
20.7428	20.4191	19.4448	80.3962

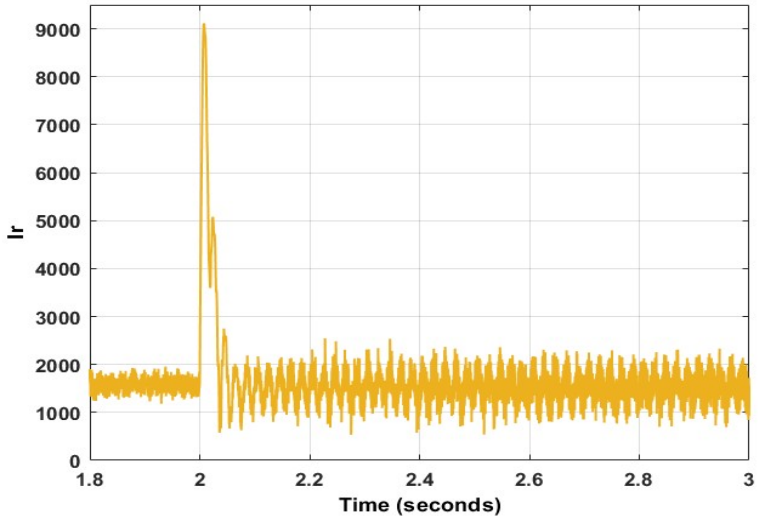

Figure 45. Rotor current transient using PI at 90% dip.

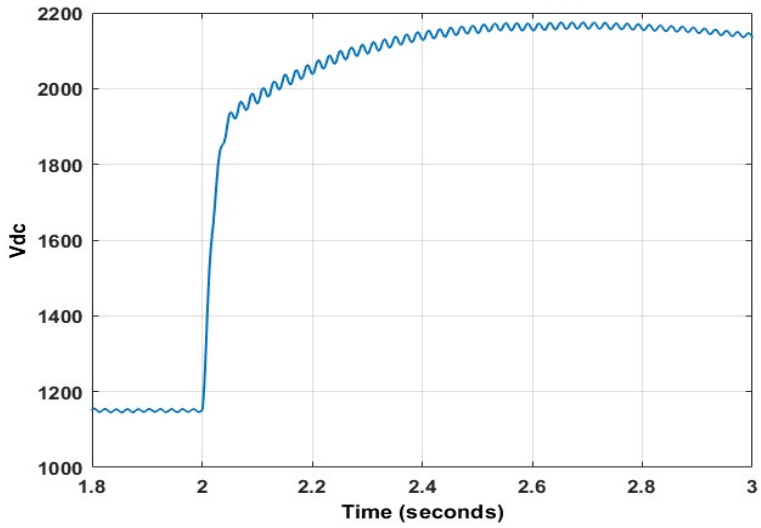

Figure 46. DC voltage transient using PI at 90% dip.

Table 9 indicates the optimized gains for the DCI, considering a voltage dip of 90%. Figures 49 and 50 represent the total rotor current magnitude and DC voltage, respectively, of the DCI. Figures 51 and 52 indicate the rotor direct axis current steady state ripple and steady state error, respectively, of the DCI. From Figure 49, the peak rotor current magnitude is observed to be 8679 A, indicating a superiority of 25.74% over the conventional PI controller. Figure 50 depicts the peak DC voltage as 2137 V, exhibiting a 18.65% better response than the PI controller. The steady-state ripple of the rotor direct axis current, as shown in Figure 51, is 667.5 A, which is 60.46% inferior to the PI controller. The average steady state value in Figure 52 is 1230.17 A. This correlates to an error percentage of 16.42%. This error is inferior to the conventional PI controller.

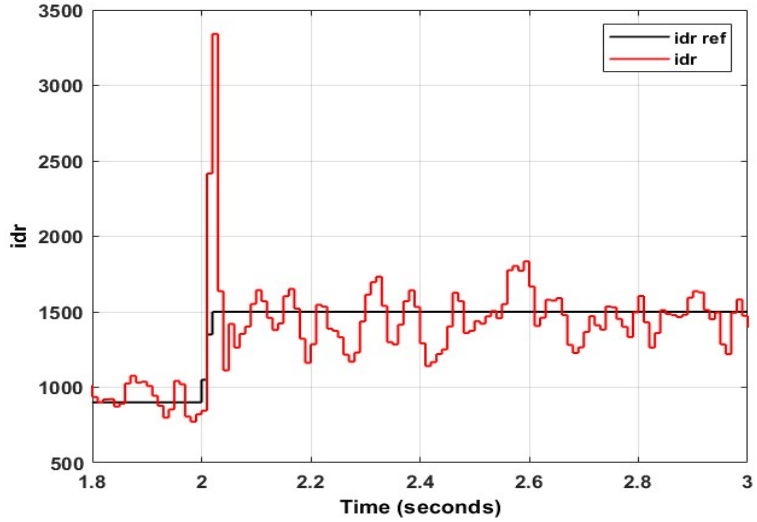

Figure 47. Rotor direct axis current ripple using PI at 90% dip.

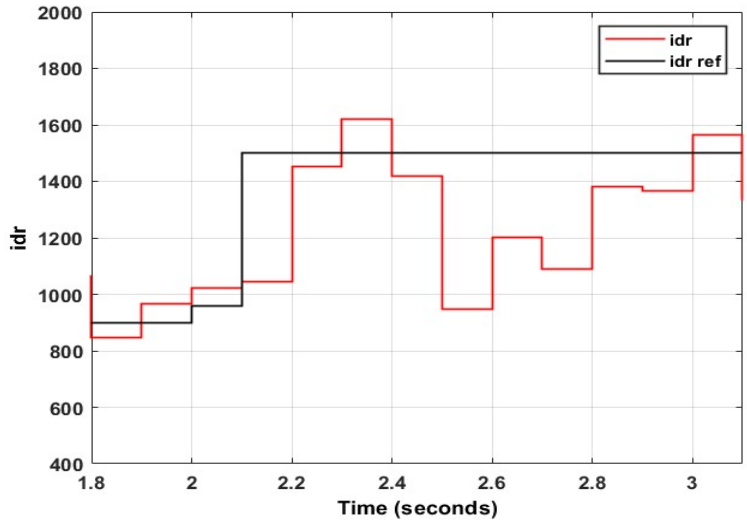

Figure 48. Rotor direct axis current average using PI at 90% dip.

Table 9. DCI controller gains at 90% dip.

K_1	K_2
100	24.3195

Table 10 indicates the optimized gains for the LQR, considering a voltage dip of 90%. Figures 53 and 54 represent the total rotor current magnitude and DC voltage, respectively, of the LQR. Figures 55 and 56 indicate the rotor direct axis current steady state ripple and steady state error, respectively, of the LQR. From Figure 53, the peak rotor current magnitude is observed to be 7245 A, indicating a superiority of 25.74% over the conventional PI controller. Figure 54 depicts the peak DC voltage as 1834 V, exhibiting a 18.65% better response than the PI controller. The steady-state ripple of the rotor direct axis current, as shown in Figure 55, is 422 A, which is 1.4% inferior to the PI controller. The average steady state value in Figure 56 is 1172 A. This correlates to an error percentage of 21.87%. This error is inferior to the conventional PI controller.

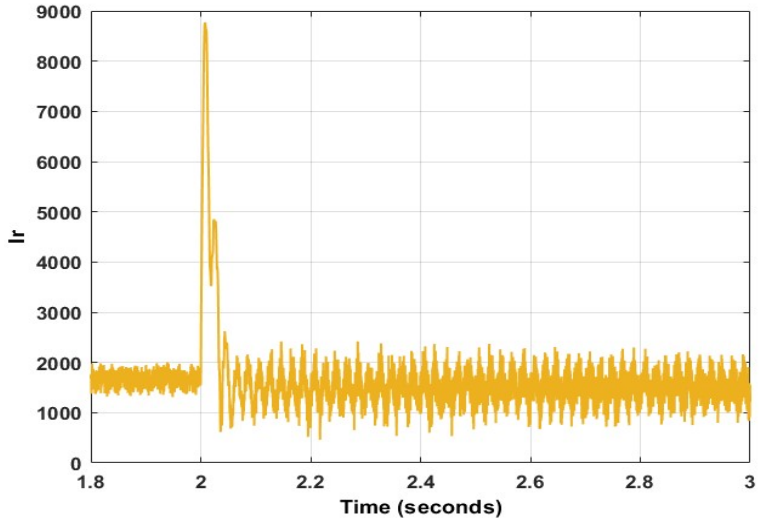

Figure 49. Rotor current transient using DCI at 90% dip.

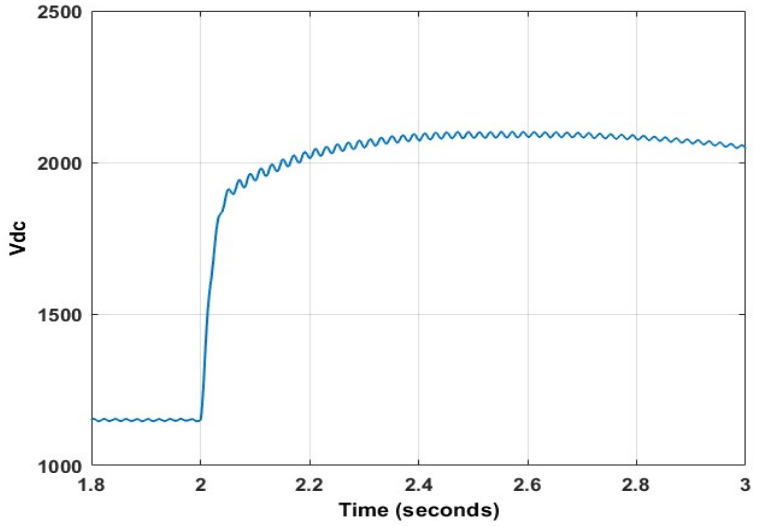

Figure 50. DC voltage transient using DCI at 90% dip.

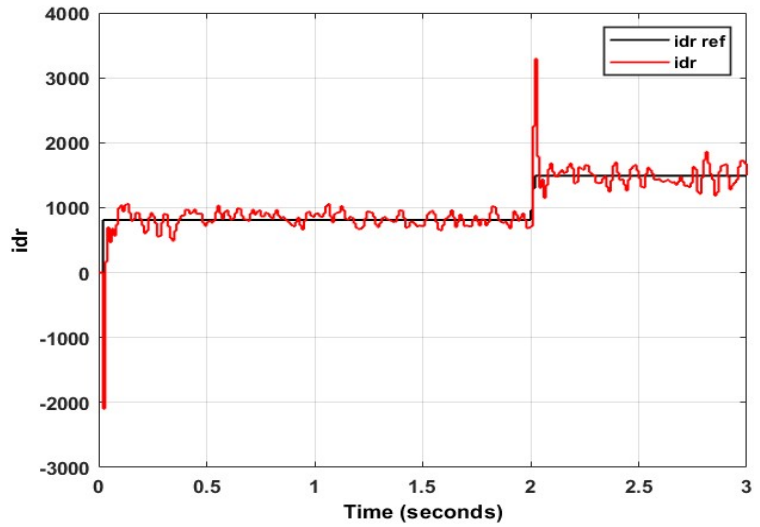

Figure 51. Rotor direct axis current ripple using DCI at 90% dip.

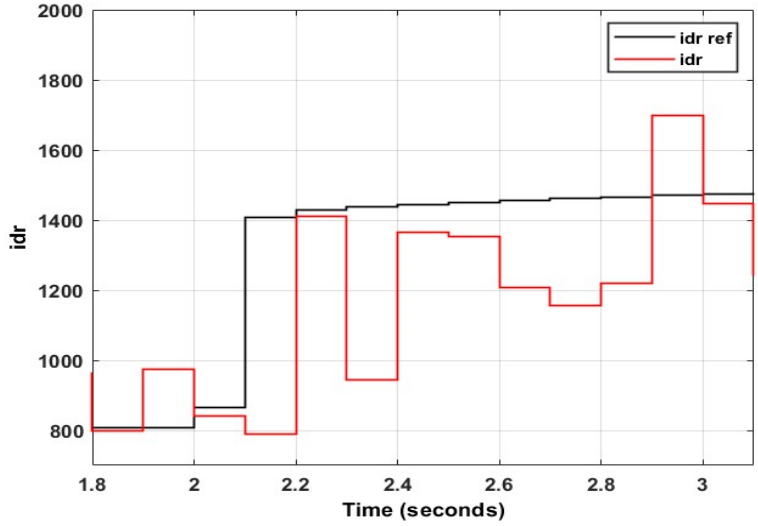

Figure 52. Rotor direct axis current average using DCI at 90% dip.

Table 10. LQR controller gains at 90% dip.

K_1	K_2	K_3	K_4
100	24.3195	44.45006	7.244542

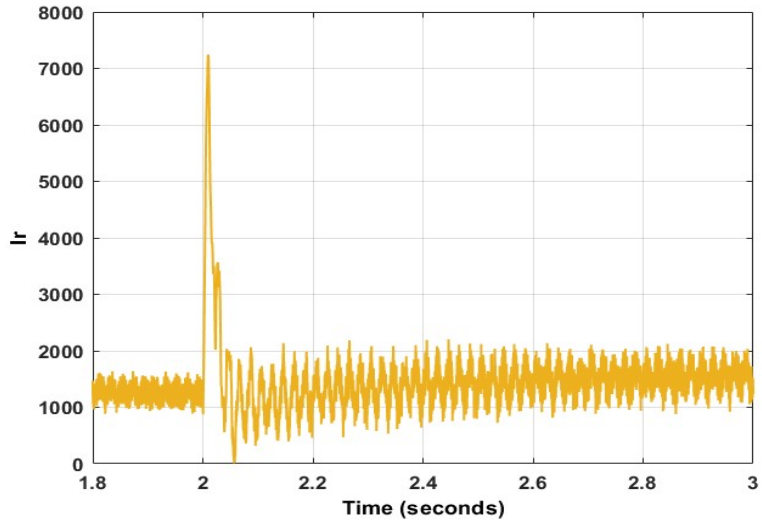

Figure 53. Rotor current transient using LQR at 90% dip.

The results of the investigation conducted are summarized in Table 11. As evident in Table 11, the LQR, coupled with a strong metaheuristic optimization technique, has obtained significantly produced better results than the conventional PI controller on most of the occasions. Superiority in terms of rotor current peak, DC voltage peak, and steady-state ripple were in the order of 67.5%, 20.35, and 57.24%, respectively. In the case of steady-state error, the PI controller seemed to produce better results.

This is expected, as the LQR is not well-suited for tracking problems. Comparison between the LQR and DCI methods, it is observed that the latter surpasses the former on only just occasions. These are for the steady-state error at 70% and 90% voltage dips. Once again, since the DCI method utilized PI controllers, the outcome is expected.

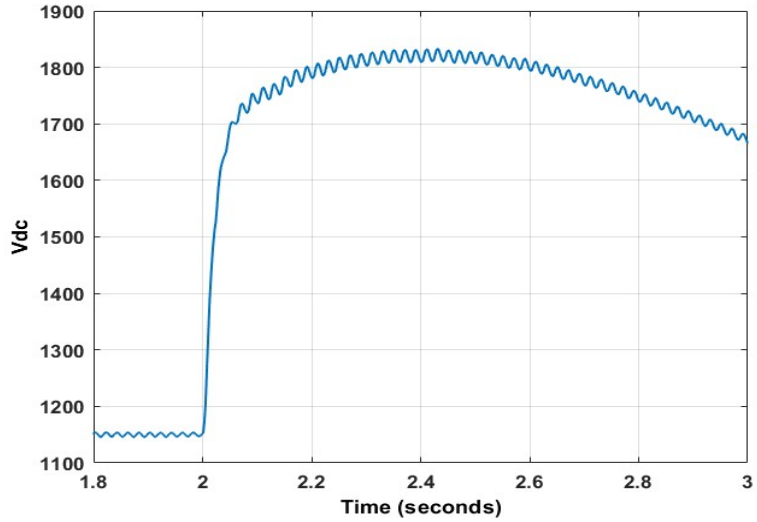

Figure 54. DC voltage transient using LQR at 90% dip.

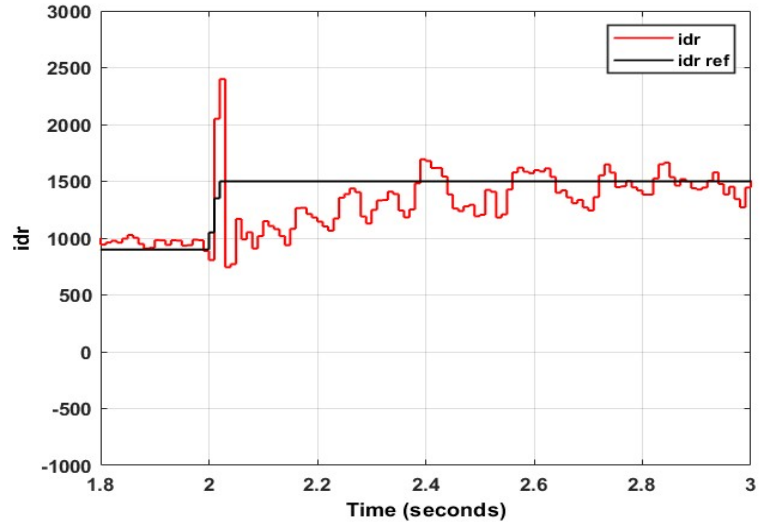

Figure 55. Rotor direct axis current ripple using LQR at 90% dip.

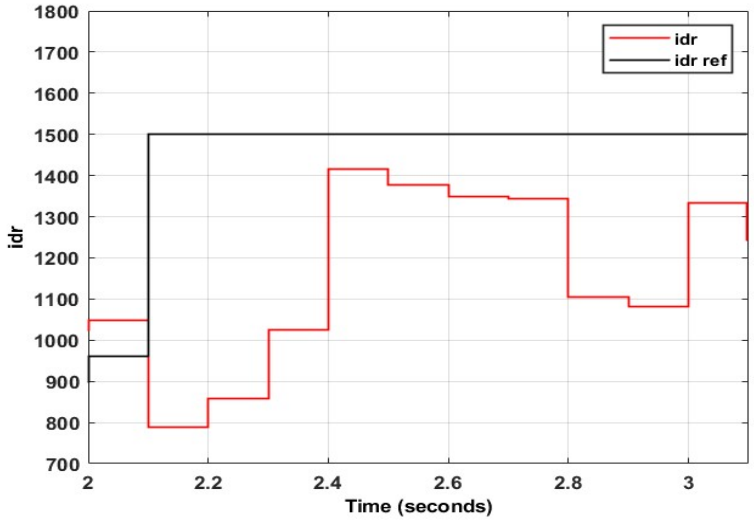

Figure 56. Rotor direct axis current average using LQR at 90% dip.

Table 11. Summary of results for PI and LQR applied to DFIG under symmetrical voltage dip.

		Rotor Current Peak (A)	DC Voltage Peak (V)	Rotor Direct Axis Current Steady-State Ripple (A)	Rotor Direct Axis Current Steady-State Error (%)
70% dip	PI	6256	1634	283	**6.07**
	DCI	5557	1597	379.5	6.89
	LQR	**3735**	**1377**	**256.5**	10.07
80% dip	PI	7550	1839	456	6.2
	DCI	7325	1787	357.5	19.74
	LQR	**4954**	**1528**	**290**	**4.87**
90% dip	PI	9110	2176	**416**	**4.3**
	DCI	8679	2137	667.5	16.42
	LQR	**7245**	**1834**	422	21.87

7. Discussion and Conclusions

This work presented an investigation into the utilization of metaheuristic optimization techniques for the control of the doubly fed induction generator under the influence of symmetrical voltage dips. Two swarm intelligence techniques were proposed; the well-known particle swarm optimization, and the recently developed African vultures optimization algorithm. These techniques were first utilized to obtain the optimal crowbar resistance for protection of the DFIG. Next, the AVOA was applied to the linear quadratic regulator for low voltage ride through of the DFIG. These results were compared to the conventional PI controller, optimized via PSO. Considering the crowbar resistance investigation, it was observed that for moderately severe symmetrical voltage dips, PSO exhibited superior results to AVOA in terms of transient magnitude, albeit the settling times were nearly identical. For severe faults (less than 80%), the AVOA exhibited dominance over PSO. This was in terms of transient magnitude, as well as settling time.

For the LVRT experiment, it was observed that the linear quadratic regulator, coupled with the AVOA, proved to be far superior to the PI controller, which was optimized using PSO. This superiority was with respect to transient magnitude and steady state ripple and was seen for almost every fault magnitude tested. However, as expected, despite the addition of the integrator, the LQR was inferior to the PI controller in terms of steady state error. Overall, it was observed that the LQR unanimously produced the best results. To further validate the effectiveness of such a controller, a 3% grid frequency perturbation was applied to the test system. Grid frequency perturbations are common occurrences with symmetrical faults, and it is therefore imperative that control systems do not lose their capabilities in such scenarios. The perturbation was applied for each of the three voltage dip magnitudes, with the results summarized in Table 12. As evident from Table 12, even when subject to grid frequency perturbations, the LQR still yielded superior rotor current and DC voltage peak magnitudes, when compared to both the PI controller and DCI methods.

Table 12. Summary of results for LQR applied subject to 3% grid frequency perturbation.

	Rotor Current Peak (A)	DC Voltage Peak (V)	Rotor Direct Axis Current Steady-State Ripple (A)	Rotor Direct Axis Current Steady-State Error (%)
70% dip	4276	1400	356	**12.4**
80% dip	5516	1585	316	13.7
90% dip	**7706**	**1873**	**417**	16.8

When comparing the results of the crowbar experiment to the results of the LVRT experiment, it is evident that in all cases, the LQR produced a superior rotor current and DC voltage transient magnitude. However, as observed in the results, the settling time of the crowbar method was unanimously better than that of the LQR. Therefore, it can be

concluded that each of these methods offer advantages and disadvantages. When coupled with powerful metaheuristic optimization techniques, these methods can be fine-tuned to produce the best possible results. Future work involves the enhancement of the linear quadratic regulator to achieve a better steady state error. This involves the utilization of the problem-specific transfer function to attempt to achieve a zero steady-state error.

Author Contributions: Conceptualization, K.R.; methodology, K.R. and A.K.S.; software, K.R.; validation, K.R. and A.K.S.; formal analysis, K.R. and A.K.S.; investigation, K.R.; resources, K.R. and A.K.S.; data curation, K.R.; writing—original draft preparation, K.R.; writing—review and editing, A.K.S.; visualization, K.R. and A.K.S.; supervision, A.K.S.; project administration, A.K.S.; funding acquisition, not applicable. All authors have read and agreed to the published version of the manuscript.

Funding: This research received no external funding.

Data Availability Statement: Not applicable.

Acknowledgments: The authors would like to acknowledge the support received from the University of KwaZulu-Natal.

Conflicts of Interest: The authors declare no conflict of interest.

References

1. Reddy, K.; Saha, A.K. Model Predictive Control of a Doubly Fed Induction Generator. In Proceedings of the 2021 Power Africa Conference, Nairobi, Kenya, 23–27 August 2021.
2. Reddy, K.; Saha, A.K. An Investigation into the Utilization of Swarm Intelligence for the Design of Dual Vector and Proportional–Resonant Controllers for Regulation of Doubly Fed Induction Generators Subject to Unbalanced Grid Voltages. *Energies* **2022**, *15*, 7476. [CrossRef]
3. Reddy, K.; Saha, A.K. A comparative study on direct torque control algorithms applied to a Doubly Fed Induction Generators. In Proceedings of the Southern African Universities Power Engineering Conference/Robotics and Mechatronics/Pattern Recognition Association of South Africa (SAUPEC/RobMech/PRASA), Potchefstroom, South Africa, 27–29 January 2021.
4. Mohamed, M.A.; Diab, A.A.Z.; Rezk, H.; Jin, T. A novel adaptive model predictive controller for load frequency control of power systems integrated with DFIG wind turbines. *Neural Comput. Appl.* **2019**, *32*, 7171–7181. [CrossRef]
5. Li, S.; Ming, Y.; Zhang, Y. Crowbar Resistance Setting and its Influence on DFIG Low Voltage Based on Characteristics. *Int. J. Robot. Autom.* **2017**, *6*, 31–38.
6. Zhou, D.; Blaabjerg, F. Optimized Demagnetizing Control of DFIG Power Converter for Reduced Thermal Stress During Symmetrical Grid Fault. *IEEE Trans. Power Electron.* **2018**, *33*, 10326–10340. [CrossRef]
7. Yan, Y.; Wang, M.; Song, Z.; Xia, C. Proportional-Resonant Control of Doubly-Fed Induction Generator Wind Turbines for Low-Voltage Ride-Through Enhancement. *Energies* **2012**, *5*, 4758–4778. [CrossRef]
8. Morsali, P.; Morsali, P.; Ghadikola, E. Analysis and Simulation of Optimal Crowbar Value Selection on Low Voltage Ride-Through Behavior of a DFIG-Based Wind Turbine. *Proceedings* **2020**, *58*, 18.
9. Zhou, Y.; Bauer, P.; Ferreira, J.; Pierik, J. Operation of Grid-Connected DFIG Under Unbalanced Grid Voltage Condition. *IEEE Trans. Energy Convers.* **2009**, *24*, 240–246. [CrossRef]
10. Kalantarian, S.R.; Heydari, H. An analytical method for selecting optimized crowbar for DFIG with AHP algorithm. In Proceedings of the Power Electronics, Drive Systems and Technologies Conference, Tehran, Iran, 16–17 February 2011.
11. Zhou, H.L.; Yang, G.; Li, D.Y. Short circuit current analysis of DFIG wind turbines with crowbar protection. In Proceedings of the International Conference on Electrical Machines and Systems, Tokyo, Japan, 15–18 November 2009.
12. Salles, M.B.C.; Hameyer, K.; Cardoso, J.R.; Grilo, A.P.; Rahmann, C. Crowbar System in Doubly Fed Induction Wind Generators. *Energies* **2010**, *3*, 738–753. [CrossRef]
13. Noureldeen, O.; Hamdan, I. A novel controllable crowbar based on fault type protection technique for DFIG wind energy conversion system using adaptive neuro-fuzzy inference system. *Prot. Control Mod. Power Syst.* **2018**, *3*, 35. [CrossRef]
14. Kondapi, K.M.; Prakash, R.B.R. Stability Enhancement of Doubly Fed Induction Generator with Virtual Resistance for Grid Disturbances. *Indian J. Sci. Technol.* **2015**, *8*, 1–7. [CrossRef]
15. Abad, G.L.J.; Rodriguez, M.; Marroyo, L.; Iwanski, G. *Doubly Fed Induction Machine*; Wiley: New Jersey, NJ, USA, 2011.
16. Senapati, M.K.; Pradhan, C.; Nayak, P.K.; Padmanaban, S.; Gjengedal, T. Modified demagnetisation control strategy for low-voltage ride-through enhancement in DFIG-based wind systems. *IET Renew. Power Gener.* **2020**, *14*, 3487–3499. [CrossRef]
17. Harandi, M.J.; Liasi, S.G.; Nikravesh, E.; Bina, M.T. An Improved Control Strategy for DFIG Low Voltage Ride-Through Using Optimal Demagnetizing method. In Proceedings of the International Power Electronics, Drive Systems and Technologies Conference, Shiraz, Iran, 12–14 February 2019.

18. Luo, J.; Zhao, H.; Gao, S.; Han, M. A Low Voltage Ride Through Strategy of DFIG based on Explicit Model Predictive Control. *Int. J. Electr. Power Energy Syst.* **2020**, *119*, 105783. [CrossRef]
19. Zhang, D.; Xu, H.; Qiao, L.; Chen, L. LVRT capability enhancement of DFIG based wind turbine with coordination control of dynamic voltage restorer and inductive fault current limiter. *PLoS ONE* **2019**, *14*, e0221410. [CrossRef] [PubMed]
20. Hazari, R.; Mannan, M.A.; Muyeen, S.M.; Umemura, A.; Takahashi, R.; Tamura, J. Stability Augmentation of a Grid-Connected Wind Farm by Fuzzy-Logic-Controlled DFIG-Based Wind Turbines. *Appl. Sci.* **2017**, *8*, 20. [CrossRef]
21. Qin, B.; Li, H.; Zhou, X.; Li, J.; Liu, W. Low-Voltage Ride-Through Techniques in DFIG-BasedWind Turbines: A Review. *Appl. Sci.* **2020**, *10*, 2154. [CrossRef]
22. Khajeh, A.; Ghazi, R. GA-Based Optimal LQR Controller to Improve LVRT. *Iran. J. Electr. Electron. Eng.* **2013**, *9*, 167–176.
23. Murari, A.; Rodrigues, L.; Altuna, J.; Potts, A.S.; Almeida, L.; Filho, A.S. A LQRI power control for DFIG tuned by a weighted-PSO. *Control Eng. Pract.* **2019**, *85*, 41–49. [CrossRef]
24. Bhushan, R.; Chatterjee, K.; Shankar, R. Comparison between GA-based LQR and conventional LQR control method of DFIG wind energy system. In Proceedings of the International Conference on Recent Advances in Information Technology, Dhanbad, India, 3–5 March 2016.
25. El-Naggar, A.; Korai, A.; Erlich, I. Using MVMO for Optimal Tuning of Linear Quadratic Regulators for DFIG-WT. *IFAC-PapersOnLine* **2015**, *48*, 479–484. [CrossRef]
26. Abdollahzadeh, B.; Gharehchopogh, F.S.; Mirjalili, S. African vultures optimization algorithm: A new nature-inspired metaheuristic algorithm for global optimization problems. *Comput. Ind. Eng.* **2021**, *158*, 107408. [CrossRef]
27. López, J.; Sanchis, P.; Roboam, X.; Marroyo, L. Dynamic Behavior of the Doubly Fed Induction Generator During Three-Phase Voltage Dips. *IEEE Trans. Energy Convers.* **2007**, *22*, 709–717. [CrossRef]
28. Patel, K.; Das, S.P. Improved Traditional Demagnetization Control of DFIG Under Balanced Grid Faults. In Proceedings of the IEEE International Conference on Power Electronics, Drives and Energy Systems, Jaipur, India, 16–19 December 2020.
29. Zhou, L.; Liu, J.; Zhou, S. Improved Demagnetization Control of a Doubly-Fed Induction Generator Under Balanced Grid Fault. *IEEE Trans. Power Electron.* **2014**, *30*, 6695–6705. [CrossRef]
30. Wu, Y.; Shu, W.; Liao, J.; Wu, W. Dynamic Behavior of the Doubly Fed Induction Generator During Three-Phase and Single-Phase Voltage Dips. In Proceedings of the IEEE 2nd International Conference on Knowledge Innovation and Invention, Seoul, Republic of Korea, 12–15 July 2019.
31. Nguyen, T.D.V.; Fujita, G. Nonlinear control of DFIG under symmetrical voltage dips with demagnetizing current solution. In Proceedings of the IEEE International Conference on Power System Technology, Auckland, New Zealand, 30 October–2 November 2012.
32. el Azri, H.; Essadki, A.; Nasser, T. LQR Controller Design for a Nonlinear, Doubly Fed Induction Generator Model. In Proceedings of the International Renewable and Sustainable Energy Conference, Rabat, Morocco, 5–8 December 2018.
33. Reddy, K. Model Predictive Control of a Doubly Fed Induction Generator. December 2020. Available online: https://researchspace.ukzn.ac.za/handle/10413/19906 (accessed on 10 October 2022).
34. Ghazi, G.A.; Hasanien, H.M.; Al-Ammar, E.A.; Turky, R.A.; Ko, W.; Park, S.; Choi, H. African Vulture Optimization Algorithm-Based PI Controllers for Performance Enhancement of Hybrid Renewable-Energy Systems. *Sustainability* **2022**, *14*, 8172. [CrossRef]
35. Fan, J.; Li, Y.; Wang, T. An improved African vultures optimization algorithm based on tent chaotic mapping and time-varying mechanism. *PLoS ONE* **2021**, *16*, e0260725. [CrossRef] [PubMed]
36. Liu, R.; Wang, T.; Zhou, J.; Hao, X.; Xu, Y.; Qiu, J. Improved African Vulture Optimization Algorithm Based on Quasi-Oppositional Differential Evolution Operator. *IEEE Access* **2022**, *10*, 95197–95218. [CrossRef]